

CIRCULATION COPY
SUBJECT TO RECALL
IN TWO WEEKS

UCRL- 97357
PREPRINT

Dynamical Models of the Barred Spiral
Galaxy NGC 3992

J. H. Hunter
R. Ball
J. M. Huntley

This paper was prepared for submittal to
The Astrophysical Journal

September 11, 1987

Lawrence
Livermore
National
Laboratory

This is a preprint of a paper intended for publication in a journal or proceedings. Since changes may be made before publication, this preprint is made available with the understanding that it will not be cited or reproduced without the permission of the author.

DISCLAIMER

This document was prepared as an account of work sponsored by an agency of the United States Government. Neither the United States Government nor the University of California nor any of their employees, makes any warranty, express or implied, or assumes any legal liability or responsibility for the accuracy, completeness, or usefulness of any information, apparatus, product, or process disclosed, or represents that its use would not infringe privately owned rights. Reference herein to any specific commercial products, process, or service by trade name, trademark, manufacturer, or otherwise, does not necessarily constitute or imply its endorsement, recommendation, or favoring by the United States Government or the University of California. The views and opinions of authors expressed herein do not necessarily state or reflect those of the United States Government or the University of California, and shall not be used for advertising or product endorsement purposes.

Dynamical Models of the Barred Spiral Galaxy NGC 3992

J. H. Hunter,¹ R. Ball,^{1,2} J. M. Huntley,³
Martin N. England,¹ and S. T. Gottesman¹

¹The Department of Astronomy, The University of Florida

²The Institute of Geophysics and Planetary Physics, University of California,
Lawrence Livermore National Laboratory

³Bell Telephone Laboratories, Whippany, NJ

Abstract

In this paper we construct dynamical models that partially reproduce observations of the HI in the barred spiral galaxy NGC 3992. The models are constrained by the large scale structure and kinematics of the gas (Paper I), and by the near infrared morphology of the bar. The dynamical components we have considered consist of (1) an axisymmetric Toomre disk of index $n=0$ and truncated as indicated in Paper I, (2) a triaxial stellar bar constrained by near infrared photometry, (3) an oval distortion of the axisymmetric disk, and (4) a spherical halo constrained by the observed kinematics and truncation of the disk (Paper I). The gas response to all or combinations of these components was investigated using the "beam scheme", hydrodynamical procedure. The strength of this approach, within the limitations of our observations, is considered in detail. Owing to the presence of the central bi-symmetry, each promising model had to be projected into the same orientation as the galaxy and then convolved with a synthetic antenna response. Only in this fashion could model and observation be compared properly.

The disk and halo components were chosen to give circular velocities in agreement with the HI kinematics. An oval distortion and/or a bar were added to produce both the observed, central deficiency in the gas and the systematic kinematic phenomena in the bar zone (the kinematic offset). The oval distortion controls the gas response at large radii but in addition, a triaxial bar, with a mass of 18-30% of the disk, must exist at the center of NGC 3992. This latter element produces the central depression and kinematic offset in the gas. Corotation of the total bisymmetric component must occur at the radius of the bar. Also, we find that a halo must surround the galaxy, containing mass roughly equivalent to that

of the disk interior to the disk radius.

We find our models suffer the major shortcoming that the gas arms of the models do not coincide with the tightly wound, star formation arms that are observed. Either the dynamics of our models are incomplete, or non dynamical causes are important to the present conjugation of the arms.

I. INTRODUCTION

In our earlier paper (Gottesman et al., 1984, hereafter Paper I) we discussed high resolution observations of the neutral hydrogen content of two barred spiral galaxies, NCG 3992 and NGC 4731. In this paper we consider the dynamical characteristics of NGC 3992.

Kinematical studies of the gas in galaxies are important, because over the large scale, the gas flow is a response to gradients in the underlying gravitational potential. In circularly symmetric systems, one can solve for the mass distribution because a unique rotation law can be constructed without difficulty. However, in non-axisymmetric systems, non-circular motions must exist. These motions add considerable complication to the problem of relating the observed motions to the dynamics, because a non-axisymmetric velocity field cannot be established solely from observed radial velocities. Hence, an alternative method, inferring velocity fields from model mass distributions, has proven extremely useful. Over the past decade, sophisticated codes of various types have been developed to model the gas response in an axisymmetric disk to the effects of a bar rotating in the disk. (Roberts, 1979 has reviewed early work, while a more recent survey is given by Prendergast, 1983.) However, until recently high quality observations with which to compare these models have been lacking. Radio studies have either been of low resolution and sensitivity (NGC 5383: Sancisi et al., 1979) or of peculiar systems (NGC 4258: van Albada, 1980). Optical observations undersample the disk of the galaxy, although they have effective resolutions of $1''$ - $2''$ (See for example Pence and Blackman 1984 a, b).

In contrast, our examination of NGC 3992 sampled completely the disk of neutral hydrogen, albeit with an average resolution of $23''$ (or 23% of the bar

length). Hence, we can describe with high precision the beam-smoothed response of the gas, at all points in the disk, to the rotating potential of the bar; we are not limited to phenomena associated with the high surface brightness regions of the bar and spiral arms. Our observations are summarized in Table 1.

NGC 3992, the galaxy we will discuss, is an intermediate range spiral of mixed ring/spiral mode. De Vaucouleurs (1959), describes these systems as having two main arms with faint additional branches near the rim of the lens. The arms of this system are thin, tightly wound, and extend (in one case) through almost 360° in azimuth. Moreover, they have been resolved into numerous nebular beads of stellar activity. In a survey of barred spiral galaxies, Elmegreen and Elmegreen (1985) described NGC 3992 as displaying prominent gas spiral arms, in contrast with the other systems which showed stellar arms. They interpreted this observation to mean that star formation in NGC 3992 has been important over the last 10^8 years. Another property of the system, that may be associated with this stellar activity, is the bright radio continuum emission from the disk. If these thin, star-formation arms are generated by shocks, the compression of the gas in the disk would enhance any magnetic field that was initially present, and increase the non-thermal brightness. Certainly of the 5 barred spiral galaxies we have observed to date (NGC 1073, 1300, 3359, 3992 and 4731), NGC 3992 has the most extensive and brightest disk in the radio continuum ($T_B \simeq 0.8 K$, $\nu = 1415 MHz$). Though less obvious, atomic hydrogen is associated with these arms, as well. Figure 1 shows a correlation of the neutral hydrogen with the optical spiral features in the outer parts of the disk, where the arms are well resolved by our synthesized beam. Similarly, in these same regions, as seen in Figure 2, velocity perturbations are visible where the line of sight traverses the optical arms. Apart from the depleted center, the apparent distribution of atomic hydrogen in a broad, patchy disk appears primarily to be an effect of our modest resolution, coupled with the

inclined disk and tightly coiled nature of the spiral arms.

In the sections that follow we will consider the nature of the bar and explore the overall ability of a particular hydrodynamic procedure, the beam scheme (Sanders and Prendergast, 1974; Huntley, 1980) to model the optical and atomic hydrogen features of NGC 3992. We will discuss the strengths and weaknesses of several models, in which the dynamical properties of a bar, disk and halo have been varied. Lastly, we will compare and discuss the observations with these models of the beam smoothed gas and velocity field distribution.

II. SURFACE PHOTOMETRY AND BAR FIGURE

Observations of the surface brightness of the bar component of an SB galaxy may be used to constrain models of its mass distribution (Stark, 1977; Ball, 1986). This information is a necessary complement to that given by the rotation curve, since for bar models the departures from axisymmetry are of primary importance. If the isophotes are modeled as a set of nested, similar ellipses, and the mass-to-light ratio within the bar is assumed constant, the derived mass distribution is a family of triaxial ellipsoids with one degree of freedom. The members of this family converge toward a single solution as the observed elongation of the bar increases. Ball (1984, 1986) has used this technique to infer the contribution of the observed bar to the potential in the SBc galaxy NGC 3359.

The case of NGC 3992 presents difficulties in the application of this method, stemming from the complexities of its isophotes in the bar region. Figure 3 presents a smoothed image of the galaxy in the I passband (λ 8250 Å), from the plate of Elmegreen (1981). This image has been given a relative intensity calibration by means of a calibration wedge, but no absolute photometry of the galaxy in this passband is available, so the flux scale remains arbitrary. The first

complication is the component at the galaxy's center, obviously rounder than the bar, which we shall call the bulge. Its presence is fairly typical for the early (SBb) type of NGC 3992. The bulge must be subtracted from the data before isophote fitting of the bar may proceed, as we will detail below. After this step has been performed, however, the brightness profile along the bar major axis remains quite anomalous. Elmegreen and Elmegreen (1985), who categorized the bar brightness profiles of 15 barred spiral into two principal types, were unable to assign NGC 3992 into either group. We believe that the remaining difficulty is caused by dust obscuring significant portions of the bar, even at these long wavelengths. The patches of dust within the bar may be seen quite clearly in the photograph shown by Sandage and Tammann (1981). Because of these two effects, there is a considerable uncertainty in trying to extract the true underlying brightness distribution of the bar of NGC 3992 from the data. We will use the photometry to establish some observational limits on the form of the bar, and then try to select a plausible model within those limits with the help of as few additional assumptions as possible.

The first step in quantitative analysis of the isophotes was convolution by a circular Gaussian beam to smooth the small-scale fluctuations of the data. The beam used had a width (FWHP) of 6.72" or two pixels, and is therefore similar to two-dimensional Hanning smoothing. These are the data displayed in Figure 3. Then, the central bulge was modeled with several different distributions. Models using both de Vaucouleurs and Hubble type profiles (cf. de Vaucouleurs and Capaccioli, 1979) were found quite unsatisfactory. The best fit, of several simple empirical expressions that were tried, was to a Gaussian distribution ($\sigma=7.0''$ after correcting for the smoothing). This component contributes 60 percent of I-band light at the galaxy center, but only 0.1 percent at a radius of 30". The orientation and ellipticity of this component are close to those expected if it is oblate (axis

ratio = 0.6) and concentric with the galaxy's disk.

The dilemma of the bulge-fitting procedure in this galaxy is well illustrated by referring to Figures 4 and 5. A model bulge having three-quarters the amplitude of the best-fit bulge was subtracted from the data, and the resulting isophotes are displayed as a contour diagram (Figure 4) and as a profile along the bar major axis (Figure 5). Although the sharp central peak has been removed by the chosen fit, the innermost contours remain obviously round, indicating that the significant contribution from the inner bulge is still present. However, the form of the brightness distribution in the bulge has been fit quite well by the model, and the only way to account for the remaining bulge light is to increase the relative amplitude assigned to the bulge component. If this enhanced bulge is computed and then subtracted from the data, the remaining brightness distribution will be more purely barlike in shape, but will have a substantial depression in brightness near the galaxy center. A bar with such a central hole hardly seems plausible in physical terms, if the brightness of this component is of stellar origin. Irregular brightness fluctuations near the center also are apparent. While one can adjust parameters to give a better fit over some selected part of the image, all bulge subtractions leave one with a bar whose radial profile fails to be monotonically decreasing. This behavior is suspect, in the context of previously published barred spiral surface photometry (e.g., Benedict, 1976; Okamura, 1978; Blackman, 1983; Elmegreen and Elmegreen, 1985). As mentioned above, the most plausible explanation is that the dust seen in the blue photograph of Sandage and Tammann (1981) obscures the I-band light from the bar, over some unknown portion of its extent. Therefore, an elaborate reconstruction of the bar volume brightness distribution from these data is not possible. The importance of these uncertainties is lessened, however, since the potential due to an extended mass distribution is given by an integral equation, and so is not very dependent on the

fine details of that distribution.

Given these limitations, we have employed the following simple approach to modeling the bar surface brightness. The orientation and extent of the bar are determined from the positions of the extreme ends of its major axis. Its apparent axial ratio β_0 is estimated from fitting ellipses to portions of the outermost contours, after subtracting the bulge as well as possible. The geometric parameters to the fit are then fixed, and only the radial brightness profile remains to be found. No unique determination of this profile is possible, but a plausible fit was created by interpolating smoothly across depressions in the "bulge-free" bar profile under the assumption that the true profile is monotonic. The resulting profile is fairly well fit by a Gaussian bar, which also has the advantage of being easily integrable. The parameters of the fit, in Stark's notation, are, for the two Euler angles, θ and ψ , 38° and 35° , respectively; $\beta_0 = 2.6''$; bar semimajor axis = $62''$ and length scale $\sigma_b = 24.''4$ for the Gaussian bar, measured along its projected major axis.

The corresponding volume brightness distribution is a single-parameter family specified by the third Euler angle ϕ . Physically, the members of this family differ in the degree to which they are flattened by the attraction of the disk. (This analysis assumes that one axis of the triaxial bar coincides with the disk rotation axis.) Mathematically, solutions are allowed which vary from having zero thickness in the disk plane to having zero thickness in a plane perpendicular to the disk. The range of possible values of ϕ is from 45.8° to 54.8° . We will assume, in the dynamical models presented below, that the shortest axis of the bar is perpendicular to the disk, so that the bars are prolate or flatter. This constraint places an upper limit of 48.4° on ϕ . The true axial ratio of the bar is 2.8 for the perfectly flat case and 1.6 for the perfect prolate case.

If the surface brightness distribution, as a function of semimajor axis a_s , is

given by the Gaussian,

$$I(a_s) = K \exp\left[-(a_s^2)/(2\sigma_b^2)\right], \quad (1)$$

one readily finds from Stark's equation (13) that the volume brightness also follows a Gaussian,

$$F_v(a_v) = \frac{K}{\sigma_b} \left(\frac{f}{2\pi}\right)^{1/2} \exp\left[-(a_v^2)/(2\sigma_b^2)\right], \quad (2)$$

where a_v is the semimajor axis of the shell (cf., Stark's equation 6).

In this equation, the geometrical factor f is defined in terms of the Euler angles and the intrinsic axial ratios (t , u). The latter are the lengths of the two bar axes that lie in the plane of disk, in units of the third axis. With the convention that $t > u$,

$$f = t^2 \sin^2 \theta \sin^2 \phi + u^2 \sin^2 \theta \cos^2 \phi + \cos^2 \theta. \quad (3)$$

For each chosen value of ϕ , a unique volume brightness distribution is specified by equation (2). Since the photometry does not have absolute calibration, the constant K is in arbitrary units. The final assumption needed to calculate model bars from this information is that the mass-to-light ratio within the bar is constant. Then the mass distribution of the bar is proportional to the volume brightness distribution of equation (2), and its potential can be calculated by adding the contributions of a set of thin, triaxial shells, or homoeoids (see equation (A 12) in the Appendix). The forces at each point of the model calculation are then computed by numerical integration of equations (A 16a) and (A 16b) over the portion of the bar which lies interior to that point. The dynamical models presented in this paper use 300 triaxial shells to approximate

the bar of NGC 3992. Clearly, this representation of the bar must be seen as one which is allowed by the photometric data, rather than required by them. However, extensive numerical experiments have shown that the response of the gaseous disk is not overly sensitive to the precise form of the bar (see also Sanders and Tubbs, 1980).

III. HYDRODYNAMIC MODELING PROCEDURES

For purposes of modeling the HI distribution in our program galaxies, we have used a 2-dimensional, Cartesian version of the gas-dynamical scheme known as the "beam scheme" (Sanders and Prendergast, 1974). While the beam scheme is only one of many numerical techniques useful for calculating 2-dimensional gas flows, we have several reasons for choosing the beam scheme to model gas flows on a galactic scale in this or any other galaxy. Some of these reasons constitute advantages which the beam scheme exhibits relative to other schemes; other reasons relate more to computational convenience or to continuity of effort, since considerable energy must be invested in the development, coding, and testing of any numerical, 2-dimensional, gas dynamical scheme. Our reasons for choosing the beam scheme are presented below.

1. The beam scheme has previously demonstrated its effectiveness in modeling gas flow on a galactic scale (Huntley, 1978; Sanders and Tubbs, 1980; Schemp, 1982).
2. The results of this scheme are consistent, in the appropriate limits, with particle orbit theory (Sanders and Huntley, 1976; Huntley, 1977).
3. Results from the beam scheme agree, to the limits of computational resolution, with the results of other 2-dimensional gas codes computing models which have the same initial conditions (Sanders, 1977; Berman,

Pollard, and Hockney, 1979).

4. When used at a typical computational resolution of 64×64 cells, this scheme provides much more than sufficient accuracy and spatial resolution to model current VLA observations of HI. The present version of the beam scheme is second-order accurate in time (time-centered, leapfrog equation-of-motion) and better than first order accurate in space, owing to the particle nature of its thermal diffusion. While the leapfrog technique strictly requires a constant time step, second order accuracy can be maintained provided that the change in the size of the time step is small between successive steps. (This result can be verified by a Taylor series expansion.) For our models, this change is at most about 2%. We note, also, that the leapfrog produces no significant change in our dynamical results over purely first order beam scheme calculations; at the resolution of our HI observations, there is no discernable difference. Van Albada (1982) compared the beam scheme with several other numerical methods and concluded that it is unsuitable for galactic gas dynamics. While we consider this work to be an excellent contribution, their conclusions have little bearing in the present context because our HI observations have such low spatial resolution (1.6 kpc) relative to the grid size of our models (0.49 kpc) that the predictions of calculations with the beam scheme are sufficiently accurate. (We have confirmed this conclusion by halving the grid size in a few models.) At higher resolutions (e.g., those of optical observations of the dust lanes, which, presumably, delineate shock fronts) the use of an improved numerical technique is warranted.
5. The beam scheme, while clearly resembling standard upwind, finite-difference schemes, also exhibits properties similar to many "particle-in-cell"

or even "smooth-particle" gas codes (Roache, 1976). This duality of properties represents a compromise in modeling between the mathematical formality of treating a continuous fluid and the physical complexity of treating a collection of diffuse HI clouds.

6. As a particle scheme, the boundary conditions are simplified. Transparent boundaries may be used for most bar-dominated models, without the need for specifying boundary values or derivatives as in implicit, finite difference schemes (cf., Liebovitch, 1978).
7. As an upwind difference scheme, the beam scheme has excellent stability properties in all regions where the gas flow is not transonic, provided that the so-called "Courant Condition" for numerical stability is met (Roache, 1976). In practice this condition was used to determine the time step.
8. In addition, the "artificial viscosity" or "diffusion terms" (numerical approximations to physical viscosity and heat conduction) are added automatically by the beam scheme at minimal levels sufficient to ensure numerical stability of the flow, even in the presence of shocks. This implicit viscosity can result in a considerable saving of computer time, relative to schemes where an explicit numerical viscosity must be added and minimized.
9. The beam scheme exists in several versions of reasonably optimized computer code. It runs efficiently in minimal storage on a 32-bit computer. Even single-precision, first-order versions of this scheme suffer no significant loss of accuracy over several galactic disk-rotations, relative to double-precision and/or second-order versions. Finally, versions of the beam scheme which include the effects of gaseous self-gravity can be made to run on a moderate-sized computer.

A 2-dimensional, Cartesian (rather than polar) version of the beam scheme was

chosen for three reasons. First, in the Cartesian version, both dimensions of all cells are the same. Hence, the effective coefficient of numerical viscosity is more nearly constant everywhere in the disk. Second, in the event of numerical artifacts in the calculations (caused, for example, by transonic flow), such artifacts would manifest themselves with Cartesian rather than polar symmetry. That is, on a Cartesian grid, numerical artifacts would not form rings or tightly-wound structures which might otherwise be mistaken for real, physical features. Third, while computing the gas flows near the center of a cartesian disk is somewhat crude, the center cell (or inner ring) of a polar grid can be particularly troublesome.

Before describing our models, we comment briefly on some of our numerical procedures. Over the past few years, we have experimented, extensively, with the beam scheme, thereby gaining experience with the variety of numerical artifacts which can arise if proper care is not taken, and in techniques for suppressing these artifacts. Guided by our experiments, we adopted the following procedures in our modeling:

1. The Cartesian reference frame in which the computations were carried out (designated hereafter as the calculational frame), was allowed to rotate rigidly at an angular speed such that co-rotation with gas in the disk of the unperturbed model would occur at a distance of 5 cell lengths beyond the outer edge of the computational grid. The model disk had a radius of 32 cells. Hence, the angular speed of the calculational frame was adjusted so that it would co-rotate with hypothetical matter, moving in circular orbits in the disk plane, at a radius of 37 cells. This procedure was adopted to minimize the artifacts of viscosity, while preventing a co-rotation resonance from arising anywhere on the model disk with the computational frame. Such computational co-rotation must be avoided, because it produces regions of

transonic flow where the stability of the beam scheme no longer is guaranteed. Our selection of computational frame has the unfortunate effect of smearing-out shock fronts, due to the motion of the bar across the grid. However, we consider this to be an acceptable compromise, because the grid size is less than one-third of the linear scale of the HI resolution.

2. The forcing terms, due to the rotating oval distortions and triaxial bars, were increased linearly with time, from zero to their final, constant values, over an interval of 100 dimensionless time steps (roughly one-half of a bar rotation period). We have verified that this turn-on procedure is gradual enough to allow the gas to adjust, quasistatically, to the noncircular forcing terms.
3. All models were allowed to evolve for at least 400 time steps (approximately 2 bar rotation periods). By that time, the gas throughout the model disks had settled into quasi-static, frame independent, trailing spiral patterns. Thereafter, due to the ubiquitous effects of numerical viscosity, each model slowly accumulated gas at its center and expelled gas through the outer boundaries of the computational grid.

During the course of the present research, we have constructed the response of the gas in NGC 3992 to various combinations of gravitational potentials. The self-gravity of the gas was not included in our models, since $M_{\text{HI}}/M_{3992} = 0.017$ and the mass of H_2 cannot be great (Paper I). Moreover, we have restricted our modeling to $r \leq 3.6'$ (14.9 kpc) from the center of the galaxy. That is the region where the spiral arms reside, and, excepting in the central "hole", the signal-to-noise ratio is high. Consequently, our models do not extend to the photometric radius, $R_{25} = 3.8'$, which is approximately the radius at which the disk mass distribution is truncated, as well (Paper I). In addition to having an axisymmetric (stellar) disk component with a central bulge, all models but one (Model 1) include

a "bar" potential, rotating rigidly in the plane of the disk, to drive the spiral arms.

In most models, the (stellar) "bar" was represented by an inhomogeneous, triaxial ellipsoid, plus an oval distortion of the surface density of the (axisymmetric) disk. In the following subsections, we summarize the characteristics of each of these mass components.

a. The Axisymmetric disks

The observed, angle-averaged, HI rotation curve of NGC 3992 rises steadily out to $r = 3.2'$ (Paper I, p. 483). Since the halo mass within R_{25} cannot exceed significantly the disk mass within that radius, and the total mass of the galaxy $4 \times 10^{11} M_{\odot}$ (Gottesman and Hunter, 1982, and Paper I), all models have included a Toomre Disk of index $n = 0$ as their disk component. When such a disk is truncated in a self-consistent fashion, Hunter, Ball, and Gottesman (1984), hereafter HBG, have designated it a Generalized Mestel Disk or GMD. Interior to truncation radius R , the circular rotation law of a GMD at distance r from its center may be expressed as,

$$V_D(r) = C \left[1 - \frac{b}{(b^2 + r^2)^{1/2}} \right]^{1/2}, \quad (4)$$

where constant shape factor b has the dimensions of length, and constant C has dimensions of velocity. The total disk mass is given by,

$$M_D(R) = \frac{2C^2 R}{\pi G} \left[1 - \frac{b}{R} \tan^{-1}(R/b) \right]. \quad (5)$$

In calculating the masses of the model disks, we have assumed that $R = R_{25} = 15.7$ kpc. (Truncation at some radius is a physical necessity, since $M_D(R)$ diverges as

$R \rightarrow \infty$). Our reasons for selecting $R = R_{25}$ are discussed in Paper I. For details on the GMD, as well as other truncated, Toomre Disks, the reader should consult HBG.

Elmegreen and Elmegreen (1985) have shown that the IR surface brightness of the disk of NGC 3992 may be approximated by the exponential distribution $I(r) = I_0 e^{-0.1479r}$, where r is in kpc. If M/L for the disk is constant, then the disk surface density would have the same shape, viz., $\Sigma(r) = A e^{-0.1479r}$. Our best models of NGC 3992 (Models 2 and 3) include identical GMD's, having a surface density very similar in shape to the above distribution outside of the bar region. The only significant disagreement between the IR surface brightness distribution and the truncated disk surface density distribution occurs near R_{25} , where the surface brightness is low. However, within R_{25} the agreement between the IR surface brightness distribution and the infinite disk surface density distribution is excellent. While mathematically convenient, our truncation procedure is arbitrary in that it was chosen to preserve the rotation field for the infinite disk for all $r \leq R$ on the finite disk. Nonetheless, to avoid orbital instabilities near the "edge", the actual truncation must be less abrupt than our model allows (for details, see HBG).

For purposes of calculating the gas responses, we have adopted surface densities $\Sigma(r)$, and interior disk masses, $M_0(r)$, appropriate for the limiting case as $R \rightarrow \infty$; i.e., we have modeled cases corresponding to interior portions of $n = 0$ Toomre Disks. The logical justification for this procedure stems from the fact that interior to the truncation radius R , the rotation curve of a GMD is independent of R . Consequently, having specified C , b , and the pattern speed of the "bar" potential, the location of co-rotation, as well as all resonances within the computing grid, are identical for both an $n = 0$ Toomre Disk and for a GMD with our selection of R . (R lies beyond the outer boundaries of the computing

grid.) The main practical reason for modeling an interior portion of a surface density distribution which extends to $r = \infty$, is that, in that case, we can use a Fourier technique to solve Poisson's Equation exactly, and in simple closed form, for the potentials and forces of multipole distortions of $\sigma_o(r)$. In particular, oval (2θ) distortions are crucial ingredients in our best models. For an $n = 0$, Toomre Disk, the expressions for $\sigma_o(r)$ and $m_0(r)$ read:

$$\sigma_o(r) = \frac{C^2}{(2\pi G)} (b^2 + r^2)^{-1/2}, \quad (6)$$

and

$$m_0(r) = \frac{C^2}{G} [(b^2 + r^2)^{1/2} - b]. \quad (7)$$

b. The Triaxial Bars

As described in Section II, the triaxial, stellar bars were modeled by superimposing 300, concentric homoeoids, having different volume densities. The volume brightnesses of the shells were required to be consistent with the surface photometry; then, volume densities were calculated by assuming a constant M/L for the mixture of stars in the bar. We justify our assumption of a constant M/L in the bar by noting that the elongated orbits of those stars are of relatively short period. Thus, the orbits of typical stars will take them to a wide variety of galactocentric radii and consequently any small volume of the bar is likely to be well mixed. This conjecture is supported by the uniformity of the color throughout the bar (Elmegreen and Elmegreen, 1985).

Using the formula derived in the Appendix, the x and y forces of each

homoeoid were calculated at each cell in the computational grid. Then, the total x and y force components due to the bar were computed at each cell by summing over the contributions of each homoeoid. (In practice, these forces were computed only once, stored, and then updated at each cell as the bar rotated relative to the computational grid.)

The degree of flattening of the triaxial bars, measured by c_t/b_t , is a free parameter in the models (b_t is the semi-minor axis of the triaxial bar in the disk plane of the galaxy and c_t is the corresponding quantity parallel to the rotation axis). We have experimented with cases, ranging from prolate figures ($c_t/b_t = 1$) to highly flattened triaxials, for which $c_t/b_t = 0.1$. Fortunately, for a fixed bar mass and pattern speed, the c_t/b_t ratio was found to have only minor influences on the gas response in an otherwise identical model.

c. Oval Distortions

Oval distortions of the axisymmetric density distribution were included in many of our models. This device enabled us to extend the non-axisymmetric forces to radii beyond those effected significantly by the observed bar. We have considered even, multiple distortions of the surface density of the form,

$$\sigma(r, \theta) = \sigma_o(r) \left[1 + A_m(r) \cos(m\theta) \right], \quad (8)$$

where $m = 2, 4, 6, \dots$. We have sought, and found, amplitude functions, $A_m(r)$, such that exact solutions of Poisson's Equation can be obtained in the disk. For a discussion of our approach, see Sanders and Huntley (1976), and Huntley, Sanders, and Roberts (1978). Although we have modeled cases which include quadrupole

($m=2$) and higher order distortions, for present purposes we restrict our consideration to a class of quadrupole or oval, distortions. For these oval distortions, the surface densities are given by ,

$$\sigma(r, \theta) = \sigma_0(r) + \sigma_{c_2}(r, \theta) = \frac{C^2}{(2\pi G)} (b^2 + r^2)^{-1/2} \left[1 + \varepsilon_{c_2} r^2 \beta^{2l} (b^2 + r^2)^{1/2} (\beta^2 + r^2)^{-(l+3/2)} \cos(2\theta) \right], \quad (9)$$

where $l=1$ or 2 , β is the length scale characterizing the distortion, and coefficient $\varepsilon_{c_2} = \varepsilon_{c_2}(t)$ gauges the amplitude of the distortion. In most of our numerical calculations, ε_{c_2} was increased linearly with t , from zero to its maximum value, over an interval of 100 dimensionless time steps. Thereafter, it was held constant at its maximum value. The potentials, corresponding to these density perturbations, read,

$$\phi_{o2} = \frac{\varepsilon_{c_2} C^2}{3} \left(\frac{r^2}{\beta^2} \right) \left\{ \frac{1 + 2(1 + r^2/\beta^2)^{1/2}}{(1 + r^2/\beta^2)^{3/2} [1 + (1 + r^2/\beta^2)^{1/2}]^2} \right\} \cos(2\theta), \quad (10)$$

and

$$\phi_{o2} = \frac{\varepsilon_{c_2} C^2}{5} \left(\frac{r^2}{\beta^2} \right) (1 + r^2/\beta^2)^{-5/2} \cos(2\theta). \quad (11)$$

For $r/\beta \gg 1$, $\phi_{o2} \sim r^{-2}$ and $\phi_{o2} \sim r^{-3}$. The perturbed r and θ force components are computed from the gradient of the potential, viz.,

$$F_{o2,r} = \left. \frac{\partial \phi_{o2}(r, \theta)}{\partial r} \right|_{\theta} \quad \text{and} \quad F_{o2,\theta} = \frac{1}{r} \left. \frac{\partial \phi_{o2}(r, \theta)}{\partial \theta} \right|_r.$$

We have experimented, extensively, with both $l=1$ and $l=2$ oval distortions. For the immediate purpose of modeling NGC3992, we need concern ourselves only

with the $l=2$ case, for which the force components $\sim r^{-4}$. This case is important in the present application in that the oval distortion must be able to modify the gas motions in the bar region, while not significantly effecting the motions in the outer disk. For the $l=2$ oval distortion, the perturbed forces are given by,

$$F_{\phi 2, r} = \frac{\epsilon_{02} C^2}{5r} \left(\frac{r^2}{\beta^2} \right) \left(2 - \frac{3r^2}{\beta^2} \right) \left(1 + \frac{r^2}{\beta^2} \right)^{-7/2} \cos(2\theta), \quad (12)$$

and

$$F_{\phi 2, \theta} = \frac{2\epsilon_{02} C^2}{5r} \left(\frac{r^2}{\beta^2} \right) \left(1 + \frac{r^2}{\beta^2} \right)^{-5/2} \sin(2\theta). \quad (13)$$

All models with oval distortions, which are shown in the tables and figures in this paper, incorporate the above formulae for calculating the perturbed forces due to the distortions. These distortions are taken to be parallel to and cororate with the bar. We have not attempted to model the response in a system for which the stellar orbits (the distortion) beyond cororation are orthogonal to the bar.

d) Spherical Halos

When spherical halos were included as a mass component in our models, then (volume) density distributions were assumed to be of the form,

$$\rho(r) = \begin{cases} \rho_c, & 0 \leq r \leq r_c \\ \rho_c \left(\frac{r_c^2}{r^2} \right), & r > r_c \end{cases}. \quad (14)$$

For radii greater than core radius r_c , the halo mass contained within radius r is given by,

$$M_H(r) = M_c \left[3 \left(\frac{r}{r_c} \right) - 2 \right], \quad (15)$$

where

$$M_c = \left(\frac{4\pi}{3} \right) \rho_c r_c^3. \quad (16)$$

In addition to the disk radius R , ten parameters fully determine each model. However, the number of parameters that can be varied freely is seven (at most), and the results are relatively insensitive to some of these. The ten parameters are: disk scale length and truncated mass, b and M_{DT} ; oval distortion length scale and amplitude, β and ϵ_{02} ; halo length scale and mass, r_c and $M_H(R)$; the bar semimajor axis, mass, flattening ratio and pattern speed, a_t , M_b , c_t/b_t and Ω_p . The apparent bar length, a_t , is fixed by the photometry, while the amount of flattening, c_t/b_t , is observationally totally indeterminate, and when specified determines the ratio b_t/a_t . The observations provide no direct information about Ω_p , and the presence of a central bulge and strong triaxial figure precludes our obtaining useful photometric data about the oval distortion component. The remaining, five parameters (bar mass plus all disk and halo quantities) are all constrained, collectively, by the observed rotation curve, the amplitude and form of which removes at least two degrees of freedom. For NGC3992, the abrupt drop in rotational velocity in the vicinity of R_{25} (the truncation "signature") may be explained by letting $M_H(R)/M_{DT} \sim 1$ (see Paper I). Similarly, the fact that the observed rotation curve does not have a central maximum, shows that $M_b/M_{DT} < 0.3$. There are additional, dynamical constraints on the triaxial bar, which will be discussed in the next section. From extensive numerical experimentation we find that the models are particularly sensitive to the parameters Ω_p , ϵ_{02} , β , and M_b/M_{DT} . Consequently, our modeling strategy has been to fix the parameters

M_{DT} , $M_H(R)$, b and r_c and then to construct models in which the above, four quantities are varied. Unfortunately, the gas response is non-linear, and usually it is impractical to vary more than one parameter at a time. In our systematic modeling, we expended considerable effort in exploring the influence of the four "sensitive" parameters, and in making the final adjustments of all model characteristics.

Before concluding this section, we address a difficulty which is inherent in deriving the angle-averaged galactic rotation curve from the observations. Apart from difficulties in measurement, particularly the necessity of using a $\cos \theta$ weighting scheme to de-emphasize the largely-transverse velocities along the minor axis (See Paper I), an important physical ambiguity remains. For a purely axisymmetric disk, the numerical value of the velocity at each radius depends on the inclination of the disk. But the shape of the rotation curve is independent of both the inclination angle i and the position angle of the line-of-nodes, PA.

For an elongated or ovaly-distorted disk galaxy with quasi-elliptical gas flow, the shape of the angle-averaged rotation-curve can depend considerably on the true orientation of the galaxy in space. For example, if we consider model 3 of Section 4, then Figure 6 shows that by varying the location of the major axis of the bar relative to the position angle of the line-of-nodes (i.e. by arbitrarily rotating the disk at a fixed inclination in space) we can radically alter the apparent, angle-averaged rotation-curve. The dependence of the observed rotation-curve on the true space angle between the bar and the line-of-nodes is therefore apparent.

For the ovaly-distorted disk, the shape of the rotation-curve at a fixed bar-to-line-of-nodes angle, BL, is still not sensitive to the inclination of the disk. However, estimation of this angle, BL, depends on the accurate estimation of i . Both PA and i can be established from observations of the outer, undisturbed

region of the disk. If these outer orbits are not nearly circular, both angles will be uncertain.

Just beyond corotation in our models, the perturbed stellar surface density giving rise to the oval distortion is 10% of the local axisymmetric disk density. While some 2θ forcing is required in order to produce spiral arms, rotation of the bar over the numerical grid in these models causes the beam scheme to overestimate the required forcing. Thus, the oval distortion in our models is an upper limit on the true magnitude of this component. In the spiral arm region of the disk, the expected velocity perturbations are substantial, amounting to ~ 20 km/sec. However, these would be reduced in magnitude at large radii. Thus, we would expect to see a systematic change in the position angle of the kinematic line of nodes with increasing radius. Such an effect, for instance, is observed in NGC 4731 (Paper I) but is not observed for NGC 3992. This offers further support to our contention that, when present, the magnitude of the oval distortion is overestimated in our models, and that both the inclination angle and line of nodes in NGC 3992 are known to at least $\pm 5^\circ$.

Thus, while we use the observed rotation curve to bound our model parameters, it is absolutely crucial that each promising model be projected into the same orientation as the observed galaxy and then be convolved through a synthetic function, which matches the response pattern of the VLA antenna configuration-i.e., the model must be "observed" as if it were the galaxy. Only then can the model radial velocities and angle-averaged rotation curve be compared, meaningfully, with those of the galaxy. We have adhered to this procedure in the present work.

In the remainder of this paper, we confine our attention to five models, containing different mass components. None, are entirely "successful", but each is the best of its class that we have been able to construct in our attempts to

simulate the gas flow in NGC3992. Characteristics of the various components of these models are summarized in Tables 2 and 3. We use the following notation:

C = asymptotic circular velocity of $n=0$ Toomre Disk in kms^{-1} ,

b = shape parameter of disk in kpc,

M_{DT} = mass of GMD in solar masses,

a_t = semi-major axis of triaxial bar, assumed oriented in the disk plane, in kpc

b_t = semi-minor axis of triaxial bar in the disk plane, in kpc,

c_t = semi-minor axis of triaxial bar perpendicular to the disk plane, in kpc,

ϕ = angle in degrees between major axis of disk isophotes and those of the bar,

M_b = mass of triaxial bar in solar masses,

ϵ_{02} = dimensionless amplitude of the $l=2$ oval distortion,

β = length scale in kpc, characterizing the $l=2$ oval distortion,

M_H = halo mass interior to $r = 14.9$ kpc in solar masses,

M_T = total mass of all components interior to $r = 14.9$ kpc in solar masses,

r_{cr} = radius at which bar would co-rotate with the undisturbed axisymmetric model in kpc.

v_{cr} = disk circular velocity at r_{cr} in kms^{-1} ($v_{cr} = \Omega_p r_{cr}$),

r_i = radius of Inner Lindblad Resonance in kpc, and

r_o = radius of Outer Lindblad Resonance in kpc.

In the next section, we present a further discussion of our modeling procedures, along with a detailed comparison of these models with the observations.

IV. THE MODELS

A number of structural and kinematical phenomena, observed in the HI data of NGC 3992, were compared with the models in order to assess the quality of their fits. In the model structure, we examined the extent, contrast and winding of the spiral arms, as well as the magnitudes of the central depressions in the gas. Also, we have insisted that a satisfactory model generate several kinematical phenomena. First, the angle-averaged model rotation curves must match the observed curve. Additionally, the magnitudes of the streaming motions across the model spiral arms should agree with the observed velocity fields. Finally, there is a marked shift in position of the velocity contours across the central, HI hole in NGC 3992 (See Paper I). This feature, the kinematic offset, also must be reproduced by a successful model. From a dynamical standpoint, we were concerned with the existence and/or location of critical resonances, which would effect the stability of the stellar bar and the location of the spiral arms. In the following paragraphs we discuss these properties and in Table 3 we summarize critical characteristics.

From Figure 1 it is clear that the observed arm-interarm HI contrast (beam-smoothed) can not be too high. In the outer regions, where our observations allow measurements to be made, we find a ratio (maximum:minimum) of 1.2 - 1.5. The arms, as characterized by their optical properties, are thin, tightly wound, and extend through the better part of one complete turn. Also, the optical arms are more complicated than simple bi-symmetry will allow. A further significant feature in the gas is the central depression in the HI. As we argued in paper I, this depression is very unlikely to be "filled" with molecular hydrogen. The upper limit on amount of H_2 inferred from CO observations is not sufficient to make up the deficit (Paper I).

It might be argued that the central hole need not be caused by dynamical effects associated with the bar. A burst of massive star formation, or some other disruptive event, in the nucleus of NGC 3992 in the relatively recent past might have depleted the gas in that region.

However, we consider such an explanation to be unlikely for several reasons. First of all, the rate of star formation near the nucleus of a spiral galaxy can be estimated from the ratios of its IRAS Point-Source Catalog fluxes. The ratio of $100\ \mu$ flux to $60\ \mu$ flux is an inverse measure of the proportion of hot dust present; in galaxies where other indicators point to a high rate of star formations, this ratio is generally less than three. One of us (R.B.) recently evaluated this ratio for a sample of 50 spiral galaxies selected to be optically large, but unbiased as to type. For NGC 3992 the flux ratio is 11.1, which is the largest value in the entire survey by over 40%. In other words, the present rate of star formation in the central $90''$ of NGC 3992 is extraordinarily low, which strongly implies both a lack of molecular gas and that star formation cannot be responsible for the gas depletion. A dynamical explanation for the depletion also is suggested by the symmetry of the hole, as well as the fact that similar holes are present in two other strongly barred galaxies that we have observed (NGC 1073 and NGC 1300). Moreover, in each case, the radius of the hole is very nearly equal to that of the optical bar, and we see no indication of disruptive phenomena at optical and infrared wavelengths. Therefore, we regard the central hole as a feature which must emerge from a "successful" dynamical model.

Figure 7 is a superposition upon an optical photograph of the galaxy the observed radial velocities minus those of a strictly circular velocity field, which matches the angle-averaged rotation field of NGC 3992 (Model 1). Systematic trends are apparent, which tell us about non-circular, streaming motions associated with the bar and with the spiral structure. Near the line of nodes,

azimuthal terms dominate, while, near the minor axis, only the radial terms can be seen in the velocity perturbations. As the magnitude and sense of these non-circular motions are dynamically related to the non-axisymmetric component of the potential, they represent important constraints on any model. Finally, as we noted in Paper I, the isopleths of constant velocity do not pass smoothly through the center of the galaxy. Such differential effects (kinematic offsets) would be expected from oval motion in and around the bar.

The non-axisymmetric mass distribution of the bar would be expected to play a leading role in generating these observed, dynamical effects in NGC 3992. However, limitations can be placed on the bar mass, since the total mass in the center of the galaxy cannot be too large. If it is excessive, the rotational velocity in the inner region will rise too rapidly. An inner maximum in the rotation law could be generated, which would fall off before rising again at larger radii. In this event, there probably would be two Inner Lindblad Resonances and the gas would be far out of phase with the stellar bar (Sanders and Huntley, 1976). However, if such an inner maximum exists in NGC 3992, it must lie within $1'$, for it is not observed. Also, for the bar to be viable, certain limits can be placed on resonances. For example, co-rotation almost certainly must occur beyond the "radius" of the bar - otherwise, it is difficult to understand how the bar could be stable (Contopoulos, Private Communication).

Our modeling strategy is summarized in the following steps.

1. Disk and halo components were selected which gave circular velocities roughly in agreement with the observed, HI rotation curve.
2. A strong oval distortion was added, having a pattern speed such that r_{cr} was somewhat $> a_t$. Then, a series of models was run in which the distortion was reduced until the "holes", adjacent to the gas bars, were of approximately the size and contrast of the observed central HI depression.

3. A triaxial bar was included, oriented parallel to and co-rotating with the oval distortion, and the disk and halo parameters were modified to correct for the bar mass.
4. The oval distortion parameters then were corrected until the optimal gas response was generated, both in the bar region and in the outer portions of the disk.
5. Finally, the bar mass was varied until the kinematic offset approached the observed value as closely as possible. This step is complicated, considerably, by the fact that several parameters must be changed simultaneously as the bar mass is varied.

Bearing in mind the various constraints imposed by the observations, we return to the models of Table 2.

a) Model 1

This model has an axisymmetric mass distribution, and may be used as a convenient standard against which the barred models may be gauged. The bar is replaced by an inhomogeneous, spherical mass distribution of radius a_t , having the same mass and extent as the triaxial bars of models 2 and 3. Figures 8 and 9 show the projected angle-averaged rotation curve and radial velocity field for Model 1. The model does not (and cannot) produce spiral arms or kinematic offsets across the "bar" region. The fact that the beam smoothed velocity residuals of Figure 7 are relatively small over most of the disk shows that any spiral structure in the gas is not well resolved and is relatively weak. This conclusion is consistent with the HI surface density maps (Figures 3a and 3b of Paper I).

b) Models 2 and 3

We regard these two models of the gas response in NGC3992 as our most successful ones. They are identical, excepting that Model 3 has a prolate bar, whereas the bar of Model 2 is a flattened figure. As mentioned previously, we find that flattening a bar has only a minor effect upon the gas response. Both models have identical halos, with $M_H(R) \sim M_{DT}$, and both have identical oval distortions. Moreover, the pattern speeds in both models are very nearly the same.

In these models, the trailing, spiral arms have a surface density > 1.2 times that of the background gas for $> 210^\circ$ in azimuth. Their average pitch angles, $i \sim 25^\circ$, are considerably greater than 10° , the approximate, average pitch angle of the tightly-wound, optical, spiral arms. Figures 10-13 show the results of Model 3. The corresponding figures for Model 2 are very similar. Both models generate satisfactory gas depressions and kinematic offsets in their bar regions. (In Model 2, the kinematic offset is slightly greater, and the hole somewhat smaller, than in Model 3). In contrast with Model 1, the velocity residuals in these models (as well as in many other of our barred models) have systematic patterns which coincide with the model arms. Notwithstanding, the departures from circular flow are relatively small (excepting in the bar region), meaning that the overall spiral structure in the gas is weak. In order to generate the desired, overall gas response, it was necessary to include a triaxial bar and oval distortion in both models. In the bar regions of these models, non-circular motions of ~ 200 km/sec developed, whereas in the arms the corresponding speeds were ~ 35 km/sec. In both models the kinematics of the bar regions agree well with the observations. It is in the arm regions that the models are less successful.

c) Model 4

Model 4 is identical with Model 3, excepting that it lacks the oval distortion component. Although the spiral arms in this model are more tightly wound ($i \sim 20^\circ$) than those of Models 2 and 3, both the contrast and extent of the arms are less than in those models. Excepting in the bar region, the velocity residuals are not large and they follow the systematic pattern as those of Model 3. The greatest defect of Model 4 is that its kinematic offset is only $\sim 60\%$ of the observed amount. In general, when an oval distortion is added to a model, the kinematic offset is increased and the arms are strengthened. (An undesirable characteristic that usually accompanies an oval distortion is the tendency to form a gas bar.) We could not increase the mass of the bar in order to produce the observed kinematic offset without generating an unacceptable rotation curve. In contrast, an oval distortion does not modify the angle averaged rotation curve.

d) Model 5

The importance of including a halo component in models of NGC3992 is illustrated by Model 5, which consists of only a disk and a prolate bar. In order to produce something resembling the observed gas response, the bar mass had to be increased to $\sim 38\%$ of the disk mass, the disk scale length increased and the pattern speed reduced. The resulting contrast and extent of the spiral arms, as well as the kinematic offset, in this model are less than those of Models 2 and 3; however, these characteristics would be increased if an oval distortion were included. The average pitch angle of the arms is 18° , a value closer to the pitch angles of the optical arms. The great shortcoming of Model 5 is that, with such a large bar mass, its angle-averaged rotation curve has a central maximum at $r \sim 1'$ (within the bar region). As mentioned previously, we did not observe this feature,

and would have seen it if it were present. When a halo is included in the model, not only can the masses of both the bar and disk be reduced, but M_B/M_{DT} can be reduced as well. In some of our models (e.g., Models 2 and 3), the spiral arms extend smoothly from co-rotation to well beyond the Outer Lindblad Resonance. Therefore, the latter resonance is not an impenetrable barrier to the arms, as has often been assumed from linear theory (Rohlfs, 1977). Important characteristics of these models are summarized in Table 3.

In the models described above, the dynamical influences of the central bulge were absorbed in the other axisymmetric components. This was done because the rotation curve appears to rise slowly, and a massive centrally condensed bulge would result in an inner maximum in the rotation curve, which would have to lie well within the HI hole. However, such a bulge could be important because it might give rise to Inner Lindblad Resonances. Therefore, we have integrated a series of models which includes bulges that are consistent with the photometry. Qualitatively speaking, the effects of the bulges in all of these models are similar; relative to Models 1 - 5 above, they exhibit greater departures from circular motions in their innermost regions, which result in stronger and more strongly offset shock fronts near their centers. Velocity vectors in the rotating bar frame are shown in Figure 15b for an extreme model with a massive bulge, assumed to have an M/L ratio equal to that of the bar. The adapted radial bulk density distribution in the bulge is Gaussian, with $\sigma = 0.58$ kpc, and the bulge mass = $0.98 M_B$. Other characteristics of this model are identical with those of Model 3, excepting that $M_H = 0.75 M_{DT}$. Shown, also, as Figure 15a are the corresponding velocity vectors for Model 3. From a comparison of these diagrams in Figure 15, it is apparent that the dynamical signature of the bulge component is confined to a region within the hole and, therefore, our HI observations can be represented satisfactorily by models in which the bulge is absorbed in the disk and halo

parameters. Thus, while a central bulge, unquestionably exists in NGC 3992, in view of the number of parameters that clearly are necessary in modeling the gas response, we have not included separate bulge components in most of our calculations.

There are many examples of barred galaxies with slowly rising rotation laws, e.g. NGC 4731 (Paper I), NGC 3359 (Cheriguene, 1975); NGC 3198 (Bosma, 1981); NGC 3054 (Rubin et al. 1982); M83 (de Vaucouleurs, Pence and Davoust, 1983). Also, Teuben and Sanders (1985) noted that there is an abrupt change between slowly rotating, dynamically hot bars and rapidly rotating, dynamically cold bars that corresponds to the disappearance of the ILR from the bar region. The lack of offset dust lanes would indicate that the bar in NGC 3992 is of the latter class, and that a resonance is not required for suitable models. Finally, we note that the three dimensional simulation of Miller and Smith (1979) formed bars that did not exhibit ILR's.

In order to converge upon these models, we carried out a large number of numerical experiments, most of which resulted in models which clearly are incompatible with the observations. For example, we established that the bar cannot reasonably be represented by only a (2θ) oval distortion, irrespective of what axisymmetric components are present. All models of this type, having co-rotation outside of the observed bar ($r_{cr} > a_t = 4.28$ kpc), resulted in an S-shaped gas distribution, with the gas bar oriented roughly parallel to the direction of the distortion. The gas could be swept out of the bar region only the pattern speeds were unacceptably large (e.g., as $r_{cr} \rightarrow 0$). When triaxial bars were included in the models, we found that the optimal pattern speeds placed r_{cr} somewhat beyond the end of the bar.

From these numerical experiments, we venture the following general remarks about the sensitivity of the models to changes in various parameters.

- a. The gas responds most sensitively to changes in the pattern speed. For example, if the Ω_p 's of Models 2 and 3 are increased by 10% the spiral arms break up into clumps; if the Ω_p 's in the models are decreased by 10%, the spiral arms become too weak and the central holes nearly disappear. These results confirm the conclusion from stellar dynamics that corotation should lie beyond the end of the bar.
- b. Having specified Ω_p , the models are least sensitive to the flattening of a bar of fixed mass and radius. This result is in agreement with the conclusions of Sanders and Tubbs (1980).
- c. The gas response is not particularly sensitive to changes in the disk and halo parameters, provided that they have been adjusted to produce a distribution of circular velocities that approximates to the observed HI rotation curve. Notwithstanding, we were unable to match the observations, even approximately, unless the halo masses in the models satisfied the condition, $0.7 M_{DT} < M_H(R) < 1.4 M_{DT}$. In view of comments b and c above, it is clear that we cannot guarantee the uniqueness of a model which fits the available observational data.

All of our bisymmetric models of this galaxy suffer the major shortcoming that the model arms do not coincide with the observed optical arms. It seems unreasonable to argue that they should not, for, as we have noted, in the outer portions of the disk (where the resolution allows) the optical and HI arms do coincide. The velocity residuals in Figure 12 have a distinctly systematic pattern, which coincides with the model arms, and is found in all of our models. The resolution of the difficulty may be related to the lack of 2θ symmetry in the outer optical arms. (One of the arms is bifurcated into two distinct and prominent

sections — thus, the galaxy displays $\sim 3\theta$ symmetry in its outer regions.) Contopoulos (1985) notes that the outer 4/1 resonance may have some observable consequences in real galaxies. We have examined the optical galaxy for any peculiarities to determine whether these coincide with the $\pm 4/1$, and $\pm 2/1$ resonances in our models. The bifurcation of one of the arms mentioned above ⁶ was of primary interest, as was the region to the NW⁷ of the nucleus, where the arm showed a break or kink. In

⁶(the east arm, $r_{\text{sky}}=1.46$; $PA_{\text{sky}}=75^\circ$)

⁷($r_{\text{sky}}=1.46$; $PA_{\text{sky}}=-42^\circ$)

models 2 and 3, co-rotation is at $r = 4.3$ kpc, the Outer Lindblad Resonance ($-2/1$), lies at 8.9 kpc and the inner and outer (\pm)4/1 resonances at 0.7 kpc and 6.6 kpc respectively. In NGC 3992, the bifurcation region is ~ 7 kpc from the center and the NW "kink" is ~ 11 kpc from the center.

The similarity in radii between the $-4/1$ resonance and the bifurcation region is intriguing. The similarity suggests that the bifurcation may be caused by the $-4/1$ resonance. However, it is not clear this interpretation is reasonable, since higher-order, even-numbered resonances should affect spiral arms on both sides of the galaxy in the same manner. If this bifurcation is to be physically associated with the $-4/1$ resonance, then "local" phenomena (e.g. cloud-cloud interactions or irregularities in the gas distribution) may have to be invoked to account for the lack of symmetry.

The NW kink lies well beyond the Outer Lindblad Resonance and probably is not associated with any of the resonances considered here. While the dust lanes in the bar region lie just beyond the inner 4/1 resonance, these lanes probably result from shock fronts along the bar at the resonance (Roberts, 1979).

By including a spiral potential, with a pitch angle of 10° , in Models 2 and 3 we have succeeded in generating model arms that are as tightly wound as the optical arms. However, then, the gas response in the bar region does not fit the observations - the hole disappears altogether and the kinematic offset is reduced greatly. We do not understand these effects fully.

If the fractions of bar to disk in both mass and luminosity are known, we can compute (M/L) for the bar, in terms of that for the disk. (In making this estimate, we ignore the small difference between our value for the disk radius and that adopted by the Elmegreens.) Elmegreen and Elmegreen (1985) have attempted to determine the fractional luminosity of the bar, relative to the disk, in their I-band surface photometry. They define the bar as the sum of the $m=2$ and $m=4$ modes in a Fourier decomposition. Their result is that the ratio of the bar to disk light is, for the disk inside $R_{25} = 3.8'$, 3.79%; and within r_{bar} , 23%. Using the values for the relative bar mass and luminosity given earlier in this section, we compute $(M/L)_{\text{bar}} = 6.9 (M/L)_{\text{disk}}$, for the disk as a whole, and $(M/L)_{\text{bar}} = 6.6 (M/L)_{\text{disk}}$ for the region within the bar radius. The accordance between these two estimates is rather heartening. It implies that the mass to light ratio for the disk component in the bar zone does not differ from that in the outer disk. However, the factor of seven enhancement of $(M/L)_{\text{bar}}$ over that of the disk is surprisingly high, but may be in error, in view of the uncertainties in the luminosities which we discuss below, and in the masses summarized in Table 2.

We believe that these numbers should not be interpreted too literally because of complications, primarily, in the observed isophotes. First, the physical significance of the $m=4$ contribution is problematic, especially given the presence of the central bulge which is not aligned with the bar axis in NGC 3992. Elmegreen and Elmegreen's Figure 11 shows that the $m=4$ mode is prominent in the central parts of this galaxy. In our own attempt to disentangle the bulge from

the bar, including a rough correction for dust absorption as described previously, we find total luminosities of the bar and bulge of 1.00 and 0.91, respectively, in arbitrary units normalized to the bar luminosity. Thus, the bulge is a major contribution to the central luminosity. Secondly, the absence of any correction for internal obscuration by Elmegreen and Elmegreen may strongly affect their estimate of the bar luminosity (again, See Sandage and Tammann, 1980). Finally, the radial brightness profile is not a simple exponential, but rather a classic example of Freeman's (1970) Type II galaxies, where the intensities at intermediate radii drop well below the inward extrapolation of the exponentials which best fit the outer disks. This may be seen from the azimuthally averaged, blue profile of the galaxy in Figure 2 of Elmegreen and Elmegreen. It is also quite pronounced in the major-axis tracing from their I data used in this paper. The brightness profile flattens abruptly as one crosses the innermost spiral arm, giving a plateau-like inner disk region similar to the one observed in NGC 7479 by Blackman (1983). This behavior makes it difficult to measure accurately, and model in a simple fashion, the integrated disk contribution.

Therefore, we believe there are effects which systematically reduce the ratios $L_{\text{bar}} / L_{\text{disk}}$ as given by Elmegreen and Elmegreen. Furthermore, as discussed below, our value for the bar mass may be too high. Hence, the discrepancy between the luminosity and mass ratio may be more apparent than real.

Unfortunately, the mass to light ratios for the bar and disk in solar units cannot be calculated from the available data, since there is no absolute calibration for the I-band photometry. The integrated (M/L) ratio for NGC 3992 in the blue was given as 9.5 by Gottesman et al. (1984). That result refers to a diameter of 8.4', slightly larger than that used in the discussion here.

Before concluding this section, we mention a theoretical difficulty associated

with the presence of strong (i.e., sufficiently elongated and massive) bars in galaxies. Dr. G. Contopoulos pointed out to us that, given the photometric constraints on its shape, the bar in NGC 3992 cannot be too massive. That is, for each triaxial figure consistent with the observations, if M_b exceeds a critical value, then the two-dimensional particle response will be stochastic. For such large M_b , quasi-periodic, two-dimensional orbits will not exist in the bar region. Therefore, if a massive bar is also highly flattened, the stellar component will respond in a manner inconsistent with the applied potential. That is, no self-consistent stellar bar will be possible. Some aspects of this problem will be considered in a joint publication with Dr. Contopoulos.

But if the bar is not too highly-flattened, then two alternatives are possible. First, three-dimensional, periodic particle orbits may be found. Second, and more likely, three-dimensional particle orbits may exist which, while not strictly periodic, are still preferentially found in certain volumes of configuration space which co-rotate with the bar. Self-consistent, numerical experiments suggest that such restricted orbits may account for the barlike modes of many three-dimensional stellar systems (Miller and Smith, 1979).

V. CONCLUSIONS

We have calculated an extensive network of hydrodynamical models of NGC 3992, in an effort to match our observations of the HI distribution and kinematics from the VLA. The essential assumption of the method is that the spiral structure in the gas is a response to the imposed potentials of the galaxy's bar, disk, and halo. Below we summarize the success and shortcomings of our program.

The behavior of the gas in these models is governed essentially by four parameters: the bar's pattern speed, the amplitude and length scale of the oval distortion, and the ratio of bar to disk mass. We experimented with a wide range of these parameters, as well as a few others not fixed by observational data which proved to be of lesser importance. The thorough investigation of the response in the space of these four parameters is complex and time-consuming, because of the problem's deep non-linearity; the result of combining moderate changes in two of the parameters often is greatly different from the sum of the responses to each change individually. Thus, it was necessary to sample a wide grid in 4-parameter space, rather than being able to infer results from an examination of the "axes" of that space. A further but, we feel, essential complication was the evaluation of each model by global criteria, rather than by looking for the best matches to single features of the observations. This insistence that a "good" model reproduce as well as possible all of the observed properties forced us to respect the internal self-consistency of the physical galaxy NGC 3992. We computed many models that were adequate representations of generic "typical" barred spirals, but which lacked essential features of the gas response in NGC 3992.

In conducting this evaluation of a model's global properties, the analysis breaks down naturally into separate considerations of the gas in the bar region and

in the outer disk. Our best models are much more satisfactory in the former, and indeed we have no really satisfactory models in the disk/arm region. Thus, let us first summarize what we have learned about the bar region from this study of NGC 3992.

We have found that the gas response is extremely sensitive to the angular pattern speed Ω_p of the tumbling bar. In fact, Ω_p is in one sense the controlling variable of the gas structure; outside a narrow range of values, it is impossible to elicit a spiral response in the gas with any combination of the other parameters. The optimum value of Ω_p varies by only a modest amount over physically extreme ranges of the other parameters. In a particular neighborhood of parameter space, including that of the best models, the variation allowed in Ω_p is no more than $\pm 10\%$.

The particular value of Ω_p that is indicated by these models is one that puts co-rotation barely beyond the end of the bar (see Table 2). Furthermore, our best models do not contain an ILR. These results are interesting, in light of the current theoretical understanding of galactic bars as summarized, for example, by Teuben and Sanders (1985). These authors propose four "dynamical rules for barred spirals", which we paraphrase: (1) bars tumble in the sense of galactic rotation; (2) co-rotation must lie outside the bar distortion; (3) strong rapidly tumbling bars are cold, and, conversely, strong slowly tumbling bars are hot; and (4) the magnitude of the bar distortion is limited to axial ratios of about 1/5, due to the onset of stochasticity well inside co-rotation. Rule 1 in this list is one of our assumptions, and we note in passing that rule 4 is verified for NGC 3992 by the photometry; indeed, NGC 3992 satisfies the criterion $b/a < 1/3$, for which Teuben and Sanders find little stochasticity. The bar of NGC 3992 appears to satisfy criterion 2, but just barely. In this regard it resembles the results of some N-body studies of purely stellar bar dynamics (e.g., Sellwood 1980). Therefore, we

believe that the bar of NGC 3992 is in the "rapidly tumbling" category of rule 3. Our suspicion is confirmed by a careful examination of the distinction drawn by Teuben and Sanders between fast and slow bars: it is a phase transition marked by the disappearance of the inner Lindblad resonances at higher Ω_p . Therefore, the absence of an ILR in our models is an additional indication that the bar of NGC 3992 has a relatively fast pattern speed and is, presumably, formed from dynamically cold stellar orbits. Perhaps the notion that barred spirals possess ILR's reflects the desire to reproduce the "archetypal" straight, offset shocks (e.g., Sanders and Tubbs 1980) which NGC 3992 does not have. As modeling of more barred spirals becomes available, it will be of considerable interest to see whether there is observational confirmation of this dichotomy in bar speeds, which presumably is correlated with Hubble type.

The mass of the bar, relative to the disk mass also is reasonably well determined by these models. This parameter plays the primary role in the dynamical expulsion of gas from the center of the galaxy, and is an important partner to the oval distortion in producing the central, kinematic offset, the most dramatic evidence of non-circular motions in the galaxy's observed kinematics and the spiral arms. These firm data on the gas response close to the bar cannot be matched by models for which $M_b < 0.18 M_{DT}$, and the most satisfactory response occurs when $M_b = 0.26 M_{DT}$. On observational grounds, M_b cannot exceed $\sim 0.3 M_{DT}$, since the rotation curve does not have a central maximum at $r \sim 1'$. As discussed in Section IV, this bar mass is rather near the stellar dynamical limit, beyond which stochasticity may begin to cause stability problems for the bar. This finding serves as a stimulus for further study of three-dimensional orbits in strongly barred potentials. While the models may be consistent in a dynamical sense, there may remain a serious problem with the M/L of the bar. (See Section IV).

In addition to the triaxial component, the galaxy must possess a "massless

bar" equivalent to our (20) oval distortion of the unperturbed disk surface density. This component is necessary in order to excite a significant response in the outer disk. In other words, it is necessary that some entity extend a significant non-axisymmetric term in the potential beyond the limits of the observed stellar bar. It is worth noting that the same conclusion was reached by Ball (1984, 1987) for the SB galaxy NGC 3359, for which (unlike the present case) the modeling matched both the bar region and the outer spiral arm response, but only with the inclusion of an oval distortion.

We have had only limited success in modeling the spiral response in the outer disk of NGC 3992. The initial impression of regular spiral structure in this object is due to the length, narrowness, and near-constant, small pitch angle of the optical arms. What the eye is less quick to note is the lack of 2θ symmetry and the bifurcations, which are beyond the scope of our approach. Given this limitation, we have required that the models have arms as long, narrow, and tightly wound as possible. In no case have we been able to generate arms as extreme in these characteristics as are the optical arms of NGC 3992.

Although we were unable to generate the proper spiral structure as judged, especially, from the higher-resolution optical arm structure, we did manage to produce spiral density waves in the gas with associated velocity perturbations of the same amplitude as those seen in the outermost part of the HI disk. We emphasize that this occurs only over a very small range of Ω_p values—a range which agrees also with theoretical expectations. For other values of Ω_p the gas response is utterly unsatisfactory. Thus, if the bar is in any way instrumental in exciting a spiral response in the gas disk of NGC 3992, it must have a pattern speed very close to our value.

We find that NGC 3992 must be surrounded by a halo which contains roughly

one disk mass interior to the disk radius. This result of our modeling reinforces that same conclusion, arrived at on strictly observational grounds (Paper I). The central bulge component, while unquestionably present, need not be included explicitly in modeling the HI response of the observed gas.

Assuming that only periodic, bisymmetric forcing terms are present, Models 2 and 3 represent our most successful attempts to simulate the gas flows in NGC 3992. Since the model spiral arms in the outer disk do not coincide with the tightly wound, star formation arms actually observed in NGC 3992, either the dynamics of our models are seriously incomplete, or the present configuration of these arms is due to other causes, such as an unusual star formation history. That is, while the large scale distribution of diffuse HI clouds must reflect the global gas-dynamical responses of the disk, the distribution of HII clouds may be governed by several other processes. In particular, local (stochastic) interactions may govern the appearance of the optical arms. Therefore, the distribution of HII clouds also may depend upon the mean life times of these clouds, as well as on their birthsite distributions (Huntley and Gerola, 1981). An additional difference between the distributions of HI and HII clouds is their local mass densities. Even though the total mass of gas in NGC 3992 is small, the dynamical effect of gaseous self-gravity depends to some degree on the local gas density. If the local density of HII regions produces a sufficiently narrow and deep potential well, the local self-gravity may dominate over the forcing of the oval distortion. In such a case, narrow spiral arms may occur in the HII distribution. These narrow arms could be tightly wound if the mass of gas is not very large compared with the mass of stars. Thus, while the HI distribution should reflect the dynamics of the underlying stellar distribution, the HII distribution, which defines the optical arms, may result from forces in addition to the background gravitational field.

Acknowledgements

We are very grateful to Debra and Bruce Elmegreen who have shared with us, very generously, their photometric data on NGC 3992. Also, we have benefitted greatly from detailed discussion with Professor George Contopoulos about the dynamics of barred spiral galaxies. The observations of NGC 3992, that we have discussed, were obtained at the VLA facility of the NRAO. The National Radio Astronomy Observatory is operated by Associated Universities, Inc., under contract with the National Science Foundation. This research was also supported, in part by NSF grant AST 81-16312. Computing at the University of Florida is supported by the North East Regional Data Center. Lawrence Livermore National Laboratory is under contract no. W-7405-ENG-48 with the U.S. Department of Energy.

Table 1

Summary of the Observed Properties of NGC 3992³

Morphological Type	SBT4
Observed V_{sys} (heliocentric)	$1045.8 \pm 0.6 \text{ kms}^{-1}$
Synthesized Resolution	$26.1 \times 20.0''$
Adopted Distance	14.2 Mpc.
Scale	$1' = 4.13 \text{ kpc}$
Photometric Diameter D_{25}	$7'.6$
Diameter of HI Disk	$8'.4$
Dimension of Optical Bar	$1.7' \times 0.5'$
Position Angle, Line of Nodes	$-111.5^\circ \pm 0.6^\circ$
Inclination Angle	$53.4^\circ \pm 0.9^\circ$
Maximum Rotation Velocity	273 kms^{-1}
Radius of Maximum Velocity	$3.1'$
Mass Within Hydrogen Disk	$22.8 \times 10^{10} \text{ Mo}$
Corrected Blue Luminosity	$2.4 \times 10^{10} L_\odot$
Atomic Hydrogen Mass	$0.38 \times 10^{10} \text{ Mo}$
M_{HI}/M (Solar Units)	0.017
M/L_B (Solar Units)	9.5
M_{HI}/L_B (Solar Units)	0.16

³ These values are taken from Paper I.

Table 2
Model Parameters

Model	1	2	3	4	5
C	247.8	247.8	247.8	247.8	289.1
b	3.72	3.72	3.72	3.72	6.51
M_{DT}	9.751×10^{10}	9.751×10^{10}	9.751×10^{10}	9.751×10^{10}	9.751×10^{10}
r_{cr}	—	4.4	4.3	4.6	5.3
a_t	4.28	4.28	4.28	4.28	4.28
c_t/a_t	1.000	0.334	1.000	1.000	1.000
c_t/b_t	1.000	0.617	0.356	0.356	0.356
M_b/M_{DT}	0.255	0.255	0.255	0.341	0.381
σ_2	—	1.847^4	1.847^4	—	—
	—	2.79^4	2.79^4	—	—
M_H/M_{DT}	0.937	0.937	0.937	0.835	—
M_T	2.138	2.138	2.138	2.122	1.374

⁴ with this choice for σ_2 and σ_1 , the maximum perturbed surface density contrast is 34 % of the unperturbed surface density at $r = 1.86$ kpc.

Table 3
Important Model Characteristics

Model	1 ⁵	2	3	4	5	Observed
r_{cr}	—	4.4	4.3	4.6	5.3	—
cr	—	236.5	222.5	247.	5252.0	—
r_i	—	—	—	0.5	0.7	—
r_o	—	8.8	9.3	8.8	11.9	—
radial extent of arms (kpc)	—	11.9	11.9	8.8	9.5	12.4
angular extent of arms ($^{\circ}$)	—	212	220	175	185	200
arm/interarm density ratio	—	1.4	1.4	1.3	1.2	1.3
size of central hole (kpc)	—	4.1x2.3	4.8x2.3	4.1x2.3	4.6x1	4.0x2.4
interarm/hole density ratio	—	3.6	3.9	3.0	3.3	3.0
kinematic offset at 10^3 kms^{-1} (kpc)	—	1.4	1.4	0.9	1.2	1.6

⁵ Model 1 was a purely circular model.

APPENDIX

In this Appendix we summarize work by two of us (J.R. Ball and J.H. Hunter) which has been used to compute the gravitational forces of the inhomogenous, triaxial bars. We wish to find the gravitational force of a homoeoid: a shell of material of constant density, bounded by two concentric, similar, triaxial ellipsoids. Let the semiaxes of the inner ellipsoid be (a, b, c) where $a \geq b \geq c$ in the directions of the Cartesian coordinates (x, y, z) respectively. The outer ellipsoid is considered to have greatest semiaxes $(a + da)$, and axial ratios equal to those of the inner figure. The foundation of our approach is laid out by MacMillian (1958). In his Section 11, he demonstrates that the force on a particle in the interior of this homoeoid is zero. We shall consider, therefore, the solution at a point (x, y, z) exterior to the homoeoid. We use the following two additional results from MacMillian. First the potential of the solid, homogenous body, which is bounded by our inner ellipsoid, is

$$V_0 = \pi G \rho a b c \int_K^{\infty} \left[1 - \frac{x^2}{(a^2+s)} - \frac{y^2}{(b^2+s)} - \frac{z^2}{(c^2+s)} \right] \left[(a^2+s)(b^2+s)(c^2+s) \right]^{-1/2} ds, \quad (A1)$$

where ρ is the mass density, and K is the largest root of the equation

$$\frac{x^2}{(a^2+K)} + \frac{y^2}{(b^2+K)} + \frac{z^2}{(c^2+K)} = 1. \quad (A2)$$

The largest root of this equation is real and positive (MacMillian, p. 52). Second, in taking partial derivatives of V_0 , the terms containing partial derivatives of K vanish.

The incremental potential dV associated with our homoeoid is

$$dV = \frac{\partial V_0}{\partial a} da. \quad (A3)$$

After considerable simplification, this becomes

$$\begin{aligned} dV = \pi G \rho b c d a \{ & 3I_1(a, b, c) - (3x^2 + a^2)I_2(a; b, c) - (3y^2 + b^2)I_2(b; a, c) \\ & - (3z^2 + c^2)I_2(c; a, b) + (x^2b^2 + y^2a^2)I_3(a, b; c) + (x^2c^2 + z^2a^2)I_3(a, c; b) \\ & + (y^2c^2 + z^2b^2)I_3(b, c; a) + 3x^2a^2I_4(a; b, c) + 3y^2b^2I_4(b; a, c) \\ & + 3z^2c^2I_4(c; a, b) \}, \end{aligned} \quad (A4)$$

where

$$I_1(l, m, n) \equiv \int_K^\infty (l^2 + s)^{-1/2} (m^2 + s)^{-1/2} (n^2 + s)^{-1/2} ds, \quad (A5a)$$

$$I_2(l; m, n) \equiv \int_K^\infty (l^2 + s)^{-3/2} (m^2 + s)^{-1/2} (n^2 + s)^{-1/2} ds, \quad (A5b)$$

$$I_3(l, m; n) \equiv \int_K^\infty (l^2 + s)^{-3/2} (m^2 + s)^{-3/2} (n^2 + s)^{-1/2} ds, \quad (A5c)$$

$$\text{and } I_4(l; m, n) \equiv \int_K^\infty (l^2 + s)^{-5/2} (m^2 + s)^{-1/2} (n^2 + s)^{-1/2} ds. \quad (A5d)$$

The ten distinct integrals appearing in equation (4) may be evaluated with the aid of formulae in Section 3.13 of Gradshteyn and Ryzhik (1980, hereafter GR). However, the formula for $I_3(b, c; a)$ equation 3.135.1 in their enumeration contains a typographical error. This integral can be evaluated by making the change of variables $\theta = \sin^{-1} \left(\frac{a^2 - c^2}{a^2 + s} \right)^{1/2}$ with the auxiliary function $p = \left(\frac{a^2 - b^2}{a^2 - c^2} \right)^{1/2}$. The transformed integral can then be found in Section 2.58 of GR, specifically using formulae 2.584.72 and 2.584.87.

With this correction, the integrals of equation (5) are specified as follows. We introduce the notations

$$\alpha \equiv \sin^{-1} \left(\frac{a^2 - c^2}{a^2 + k} \right), \quad (A6a)$$

$$g_i \equiv (a^2 - b^2)^{-1}, \quad (A6b)$$

$$g_2 \equiv (b^2 - c^2)^{-1}, \quad (A6c) \quad g_3 \equiv (a^2 - c^2)^{-1}, \quad (A6d)$$

$$h_1 \equiv (a^2 + \kappa)^{1/2}, \quad (A6e) \quad h_2 \equiv (b^2 + \kappa)^{1/2}, \quad (A6f)$$

$$\text{and } h_3 \equiv (c^2 + \kappa)^{1/2} \quad (A6g)$$

The solutions for the integrals depend on the assumption $a > b > c$, and that $\kappa > 0$.

Then,

$$I_1(a, b, c) = 2g_2 F(\alpha, p), \quad (A7a)$$

$$I_2(a; b, c) = 2g_1 g_3 [F(\alpha, p) - E(\alpha, p)], \quad (A7b)$$

$$I_2(b; a, c) = 2g_3^{-1} g_1 g_2 E(\alpha, p) - 2g_1 g_3 F(\alpha, p) - 2g_2 h_3 h_1^{-1} h_2^{-1}, \quad (A7c)$$

$$I_2(c; a, b) = -2g_2 g_3 E(\alpha, p) + 2g_2 h_2 h_1^{-1} h_3^{-1}, \quad (A7d)$$

$$I_3(a, b; c) = 2g_2 g_1 g_3^2 [(a^2 + b^2 - 2c^2) E(\alpha, p) - 2g_2^{-1} F(\alpha, p)] \\ - 2g_1 g_2 h_3 h_1^{-1} h_2^{-1}, \quad (A7e)$$

$$I_3(a, c; b) = 2g_1 g_2 g_3^2 [(2b^2 - a^2 - c^2) E(\alpha, p) - g_2^{-1} F(\alpha, p)] \\ + 2g_2 g_3^2 h_2 h_1^{-1} h_3^{-1}, \quad (A7f)$$

$$\begin{aligned} I_3(b, c; a) = & 2g_1 g_2^2 g_3 \left[g_2^{-1} F(\alpha, p) - (2a^2 - b^2 - c^2) E(\alpha, p) \right] \\ & + 2g_2^2 h_1^{-1} h_2^{-1} h_3^{-1} (b^2 + c^2 + 2\kappa), \end{aligned} \quad (A7g)$$

$$\begin{aligned} I_4(a; b, c) = & (2/3) g_1^2 g_2^2 g_3 \left[(3a^2 - b^2 - 2c^2) F(\alpha, p) - 2(2a^2 - b^2 - c^2) E(\alpha, p) \right] \\ & + (2/3) g_3^2 g_1 h_3 h_2 h_1^{-3}, \end{aligned} \quad (A7h)$$

$$\begin{aligned} I_4(b; a, c) = & (2/3) g_1^2 g_2^2 g_3 \left[2g_3^{-2} (a^2 + c^2 - 2b^2) E(\alpha, p) + g_2^{-1} (3b^2 - a^2 - 2c^2) F(\alpha, p) \right] \\ & - (2/3) \left[3a^2 b^2 - a^2 c^2 + 2b^2 c^2 - 4b^4 + \kappa (2a^2 - 3b^2 + c^2) \right] g_1^2 g_2^2 h_3 h_1^{-1} h_2^{-2}, \end{aligned} \quad (A7i)$$

$$\begin{aligned} \text{and } I_4(c; a, b) = & (2/3) g_2^2 g_3^2 \left[2(a^2 + b^2 - 2c^2) E(\alpha, p) - g_2^{-1} F(\alpha, p) \right] \\ & + (2/3) \left[a^2 b^2 - 3a^2 c^2 - 2b^2 c^2 + 4c^4 - \kappa (2a^2 + b^2 - 3c^2) \right] g_3^2 g_2^2 h_2 h_1^{-1} h_3^{-3}, \end{aligned} \quad (A7j)$$

where $F(\alpha, p)$ and $E(\alpha, p)$ are the incomplete elliptic integrals of the first and second kinds, respectively. Table A1 gives the specific formulae from GR used in evaluating these integrals, except for $I_3(b, c; a)$, which, as described above, had to be evaluated somewhat more laboriously.

It is clear that we may rewrite the potential dV as

$$dV = \pi G \rho b c da \left[P F(\alpha, p) + Q E(\alpha, p) + R \right]. \quad (A8)$$

The functions P , Q , and R can be obtained by combining equations (A4), (A7), and (A8).

Upon replacing the g 's and h 's by their definitions in terms of a , b , c , and κ and manipulating the resulting expressions, we arrive at the general results:

$$P = 4g_3, \quad (A9)$$

$$Q = 0, \quad (A10)$$

$$\text{and } R = 0. \quad (A11)$$

The evaluation of R relies upon the definition of χ . After utilizing equations (A6d) and (A8), we obtain the very simple form for the potential:

$$dV = 4\pi G\rho bc da (a^2 - c^2)^{-1/2} F(\chi, p), \quad (A12)$$

a result first proved by Chandrasekhar (1969) in an entirely different fashion.

In the oblate limit ($a = b$), we have $p = 0$, and the elliptic integral $F(\chi, p)$ becomes simply χ . If we further restrict ourselves to points in the equatorial plane of the spheroid, $z = 0$, then $\chi = r^2 - a^2$, where $r^2 = x^2 + y^2$. The potential becomes, from (A6a) and (A12),

$$dV = 4\pi G\rho a e^{-1} (1 - e^2)^{1/2} da \sin^{-1}(ae/r), \quad (A13)$$

where we have defined $e = (a^2 - c^2)^{1/2}a^{-1}$. Equation (A13) is the familiar expression for an oblate shell (Mestel, 1963). The prolate form, which is very similar to this, can be recovered by interchanging c and a , and using the identities $(a^2 - c^2)^{1/2} = i(c^2 - a^2)^{1/2}$ and $-i \sin^{-1} i\theta = \sinh^{-1} \theta$ (MacMillian, 1958, p. 63).

An even further simplification ensues when the forces are computed. It arises because the position (x, y, z) enters into (A12) only through the argument χ of the elliptic integral. Therefore, by the definition of $F(\chi, p)$ (e.g., GR, p. 904), the x component of the force, for example becomes:

$$dF_x = 4\pi G\rho bc (a^2 - c^2)^{-1/2} da \frac{\partial}{\partial x} \int_0^{\sin \chi} (1 - t^2)^{-1/2} (1 - p^2 t^2)^{-1/2} dt. \quad (A14)$$

Recalling the definition of χ in equation (A6a), we obtain

$$dF_x = -2\pi G\rho bc da (1 - \sin^2 \chi)^{-1/2} (1 - p^2 \sin^2 \chi)^{-1/2} (a^2 + \chi)^{-3/2} \frac{\partial \chi}{\partial x}, \quad (A15)$$

or,

$$dF_x = -2\pi G \rho b c d a [(a^2 + \kappa)(b^2 + \kappa)(c^2 + \kappa)] \frac{\partial \kappa}{\partial x}, \quad (\text{A16a})$$

and similarly,

$$dF_y = -2\pi G \rho b c d a [(a^2 + \kappa)(b^2 + \kappa)(c^2 + \kappa)] \frac{\partial \kappa}{\partial y}, \quad (\text{A16b})$$

$$\text{and } dF_z = -2\pi G \rho b c d a [(a^2 + \kappa)(b^2 + \kappa)(c^2 + \kappa)] \frac{\partial \kappa}{\partial z}. \quad (\text{A16c})$$

The only difficulty in computing the force, then, is the evaluation of κ and of $\frac{\partial \kappa}{\partial x}$, etc. In the general case, κ is the greatest root of equation (A2), whose coefficients are functions of (a, b, c) and (x, y, z) and can be found by application of standard techniques (e.g., Abramowitz and Stegun, p. 17) at each point (x, y, z) . Implicit differentiation of the cubic equation readily yields analytical expressions for the partial derivatives of κ in terms of (a, b, c) , (x, y, z) , and κ . Therefore, after one has solved for κ , evaluation of the three force components is straightforward. Here we illustrate the procedure in the simpler case, where the point of evaluation is in one of the planes of symmetry of the homoeoid, say $z = 0$. In this case, κ is the larger root of the quadratic

$$\frac{x^2}{(a^2 + \kappa)} + \frac{y^2}{(b^2 + \kappa)} = 1. \quad (\text{A17})$$

Therefore,

$$\kappa = \left\{ (x^2 + y^2) - (a^2 + b^2) + \sqrt{[(x^2 + y^2) - (a^2 + b^2)]^2 - 4(a^2 b^2 - x^2 b^2 - y^2 a^2)} \right\} / 2. \quad (\text{A18})$$

Defining $r^2 = x^2 + y^2$ and $l^2 = a^2 - b^2$, this can be rearranged to read:

$$K = \left\{ r^2 - (a^2 + b^2) + [r^4 + l^4 - 2l^2(r^2 - 2y^2)]^{1/2} \right\} / 2. \quad (\text{A19})$$

Differentiation with respect to x gives,

$$\frac{\partial K}{\partial x} = \left\{ 1 + (r^2 - l^2) [r^4 + l^4 - 2l^2(r^2 - 2y^2)]^{-1/2} \right\} x, \quad (\text{A20})$$

which simplifies to,

$$\frac{\partial K}{\partial x} = \left(\frac{2K + 2b^2}{2K + a^2 + b^2 - r^2} \right) x. \quad (\text{A21})$$

Similarly,

$$\frac{\partial K}{\partial y} = \left(\frac{2K + 2a^2}{2K + a^2 + b^2 - r^2} \right) y. \quad (\text{A22})$$

The system of equations consisting of (A16a), (A16b), (A19), (A21), and (A22) makes the exact computation of the force due to a triaxial homoeoid very easy, therefore, in one of its principal planes. Equations (A16) are equally valid outside of the planes of symmetry. In that case K , being the root of a cubic equation, is more cumbersome to write explicitly. Once it has been found, however, equations for $\frac{\partial K}{\partial x}$, $\frac{\partial K}{\partial y}$, and $\frac{\partial K}{\partial z}$ can be written which are similar in form to (A21) and (A22). Then, by numerical integration of equations (A16a-A16c), the forces due to mass density distribution $\rho(a)$ can be calculated to a specified degree of accuracy, provided only that $\rho(a)$ is constant on triaxial surfaces.

Table A1

Evaluation of Integrals from Gradshteyn and Ryzhik (1980)

<u>Integral</u>	<u>GR Formula</u>
$I_1(a, b, c)$	3.131.1
$I_2(a; b, c)$	3.133.1
$I_2(b; a, c)$	3.133.7
$I_2(c; a, b)$	3.133.13
$I_3(a, b; c)$	3.135.9
$I_3(a, c; b)$	3.135.5
$I_4(a; b, c)$	3.134.1
$I_4(b; a, c)$	3.134.7
$I_4(c; a, b)$	3.134.13

BIBLIOGRAPHY

- Abramowitz, M, and Stegun, I.A.: eds. 1965, "Handbook of Mathematical Functions," (New York: Dover).
- Ball, R. 1986, In preparation.
- Ball, R. 1984, Ph. D. Dissertation, University of Florida.
- Benedict, G. F. 1976, A.J., 81, 799.
- Berman, R. H. Pollard, O. J. and Hockney, R. W. 1979, Astr. Ap., 78, 133.
- Blackman, C. P. 1983, Mon. Not. Roy. Ast. Soc., 202, 379.
- Bosma, A. 1981, A.J., 86, 1791.
- Chandrasekhar, S. 1969 "Ellipsoidal Figures of Equilibrium," (New Haven: Yale University Press).
- Cheriguene, M.F. 1975, in "La Dynamique des Galaxies Spirales", ed. L.Weliachew (Paris: CNRS) pp 439-482.
- Contopoulos, G. 1985, Comments in Astrophysics, XI, 1.
- De Vaucouleurs, G. and Capaccioli, M.; 1979, Ap.J. Suppl., 40, 699.
- De Vaucouleurs, G., Pence, W.D. and Davoust, E. 1983, Ap.J. Suppl., 53, 17.
- De Vaucouleurs, G. 1959, "Handbuch der Physik," ed. S. Flugge (Berlin:Springer) pp. 275-310.
- Elmegreen, B. G. and Elmegreen, D. M. 1985, Ap.J., 288, 438.
- Elmegreen, D. M. 1981, Ap.J. Suppl., 47, 229.
- Freeman, K. C. 1970, Ap.J.; 160, 811.
- Gottesman, S. T. Ball, R. Hunter, J. H. and Huntley, J. M. 1984, Ap.J., 286, 471 (Paper I).
- Gottesman, S.T. and Hunter, J.H. 1982, Ap. J., 260, 65.
- Gradshteyn, I. S. and Ryzhik, I. M. (1980), "Tables of Integrals, Series, and Products," (New York: Academic Press).

- Hunter, J. H. Ball, R. and Gottesman, S. T. 1984, Mon. Not. Roy. Ast. Soc., 208, 1.
- Huntley, J. M., Sanders, R. H. and Roberts, W. W 1978, Ap.J., 221, 521.
- Huntley, J. M. and Gerola, H. 1981, Ap.J., 248, L69.
- Huntley, J. M. 1977, Ph.D. Dissertation, University of Virginia.
- Huntley, J.M. 1978, Ap. J., 225, L101.
- Huntley, J. M. 1980, Ap.J., 238, 524.
- Liebovitch, L. S. 1978, Ph.D. Dissertation, Harvard University.
- MacMillian, W. D. 1958, "Theoretical Mechanics: The Theory of the Potential,"
(New York: Academic Press).
- Mestel, L. 1963, Mon. Not. Roy. Ast. Soc., 126, 553.
- Miller, R. H. and Smith, B. F. 1979, Ap.J., 227, 785.
- Okamura, S. 1978, Pub. Astron. Soc. Japan, 30, 91.
- Pence, W. D. and Blackman, C. P. 1984a, Mon. Not. Roy. Ast. Soc., 207, 9.
- Pence, W. D. and Blackman, C. P. 1984b, Mon. Not. Roy. Ast. Soc., 210, 547.
- Prendergast, K. H. 1983, "Internal Dynamics and Kinematics of Galaxies," ed. E.
Athanasoula (D. Reidel: Dordrecht), pp. 215-220.
- Roache, P. J. 1976, "Computational Fluid Dynamics," (Revised edition,
Albuquerque: Hermosa).
- Roberts, W. W. 1979, "Photometry, Kinematics and Dynamics of Galaxies," ed.
D.S. Evans (Austin: Univ. of Texas).
- Rohlf, K. 1977, "Lectures on Density Wave Theory," Lecture Notes in Physics,
No. 69, (Berlin: Springer).
- Rubin, V.C., Ford, W.V. and Thonnard, N. 1982, Ap. J., 261, 439.
- Sancisi, R., Allen, R. J. and Sullivan, W. T. 1979, Astr. Ap., 78, 217.
- Sandage, A. Tammann, S. A. 1981, "A Revised Shapley-Ames Catalog of Bright
Galaxies," (Washington: Carnegie Institute of Washington).

Sanders, R. H. and Tubbs, A. D. 1980, Ap.J., 235, 803.

Sanders, R. H. and Huntley, J. M. 1976, Ap.J., 209, 53.

Sanders, R. H. 1977, Ap.J., 217, 916.

Sanders, R. H. and Prendergast, K. H. 1974, Ap.J., 188, 489.

Schemp, W. V. 1982, Ap.J., 258, 96.

Sellwood, J.A. 1980, Astr. Ap., 89, 296.

Stark, A. A. 1977, Ap.J., 213, 368.

Teuben, P.J. and Sanders, R.H. 1985, Mon. Not. R. astr. Soc., 212, 257;Erratum
214, 319.

Van Albada, G. D. 1980, Astr. Ap., 90, 123.

Van Albada, G.D. 1985, Astr. Ap., 142, 491.

Figure Captions

Figure 1: Observed column density of HI in NGC 3992. The observed peak density is $1.7 \times 10^{21} \text{cm}^{-2}$. The first contour is at 50% of this peak, with successive contours at multiples of 10%. The photograph is reproduced from "A Revised Shapley-Ames Catalog of Bright Galaxies" (Sandage and Tammann 1981) and several reference stars are marked.

Figure 2: Contours of line-of-sight velocity (heliocentric) in NGC 3992. The contour interval is 20 km s^{-1} , and every fifth contour is labeled with its velocity. The photograph is from "A Revised Shapley-Ames Catalog of Bright Galaxies" (Sandage and Tammann 1981). An irregular outline in the center of the figure is the boundary of a zone where the detected HI signal is very weak. Within this area the data have been spatially smoothed to improve the sensitivity. The crosses mark the positions of reference stars. The half-power beam is shown, along with equatorial coordinates for epoch 1950.0.

Figure 3: Contour representation of the smoothed I passband image of NGC 3992 (Elmegreen 1981). The first contour is at 10% of the peak observed brightness, with successive contours at multiples of 10%. Reference positions are marked by crosses.

Figure 4: Contour representation of the I passband image of NGC 3992 after removal of a central bulge component. Contour levels are at 10% of the peak.

Figure 5: Major-axis brightness profile of I passband image after removal of a central bulge component. Brightness units are arbitrary.

Figure 6: Dependence of the angle-averaged rotation-curve and velocity field on the angle between the bar and the line-of-modes, θ . The dependence is shown for Model 3 of Section 4, with $\theta = 0^\circ$ and 90° . The velocity field contours are plotted at 20km/sec intervals.

Figure 7: Observed radial velocities minus those of a strictly circular velocity field matching the angle-averaged rotation field of NGC 3992. The photograph is reproduced from "A Revised Shapley-Ames Catalog of Bright Galaxies" (Sandage and Tammann 1981). Reference positions are marked by crosses. Contours are numbered in units of 5 km/sec.

Figure 8: Projected angle-averaged rotation curve for Model 1; axisymmetric mass distribution. The observed angle-averaged rotation curve is indicated by crosses and some typical error bars are indicated.

Figure 9: Radial velocity field for Model 1; axisymmetric mass distribution. Contours are plotted every 40 km/sec.

Figure 10: Radial velocity field for Model 3; prolate bar model. Contours are plotted every 40 km/sec.

Figure 11: Projected angle-averaged rotation curve for Model 3; prolate bar model. The observed angle-averaged rotation curve is indicated by crosses and some typical error bars are indicated. The positions of co-rotation (CR) and the Outer Lindblad Resonance (OLR) are indicated. No Inner Lindblad Resonances exist.

Figure 12: Observed radial velocity field minus those of Model 3; prolate bar model. Contours are labeled in units of 5 km/sec.

Figure 13: Model 3, prolate bar model, density contours. Contour levels are plotted at 10% of the peak and successive contours at multiples of 10%.

Figure 14: Gray scale representation of the resultant density for Model 3, the prolate bar model.

Figure 15: Velocity vectors in the rotating, bar frame for two models of NGC 3992. Figure (a) is Model 3, while Figure (b) includes a central bulge. The bar length and position are shown as solid straight lines, the dashed show the locations of the shock fronts, and the Gaussian radius of the bulge, σ , is shown as a solid, circular arch. In each diagram, the bars rotate in a clockwise direction.

Current Addresses

R. Ball: Institute for Geophysics and Planetary Physics, L-413, Lawrence
Livermore National Laboratory, PO Box 808, Livermore, CA 94550

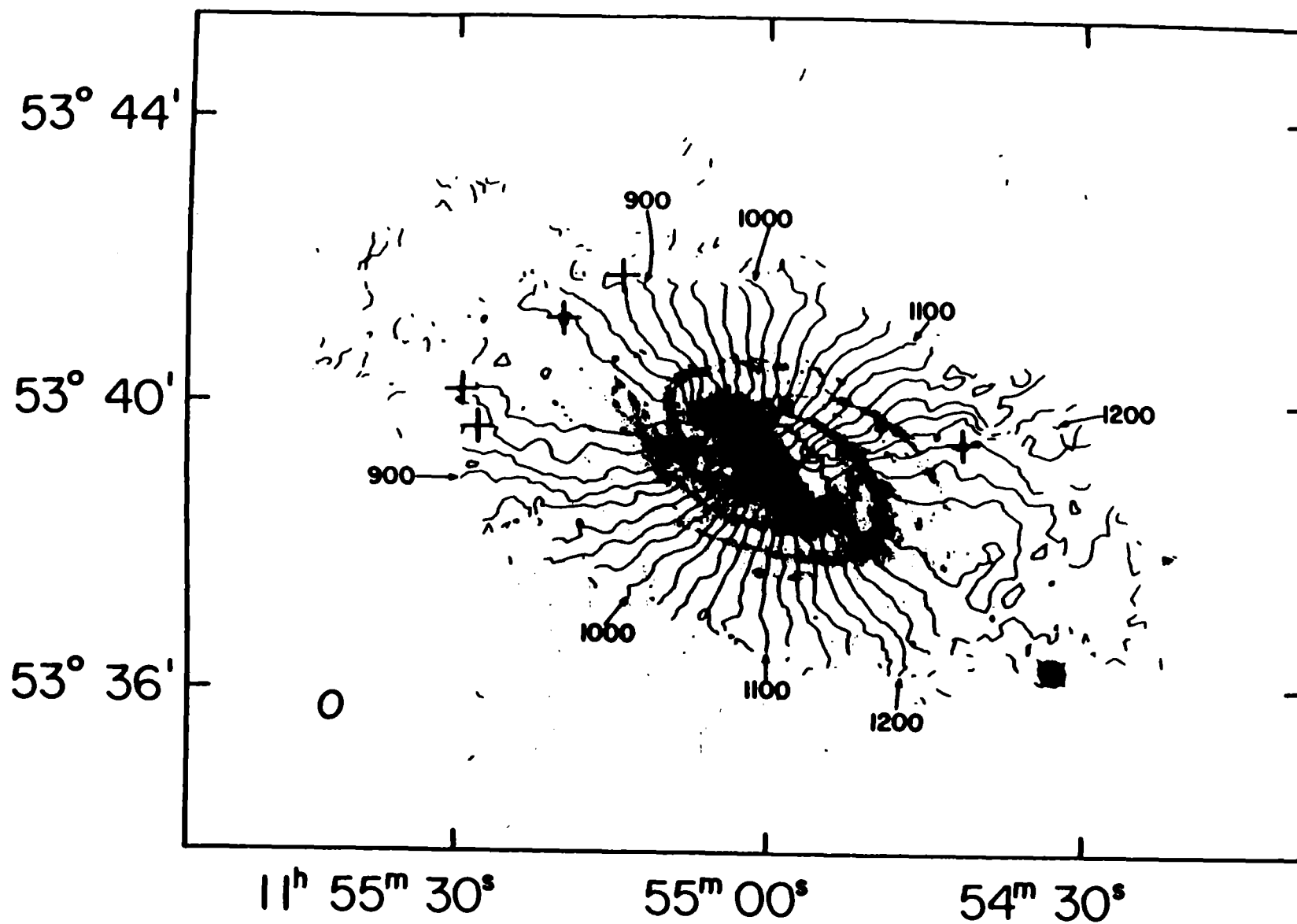
M.N. England: Interferometrics Inc., 8150 Leesburg Pike, Suite 1400, Vienna VA
22180

S.T. Gottesman, and J.H. Hunter, Jr.: Department of Astronomy, The University
of Florida, Gainesville, FL 32611

J.M. Huntley: Bell Telephone Labs., Whippany Road, Whippany, NJ 07981



Fig 1



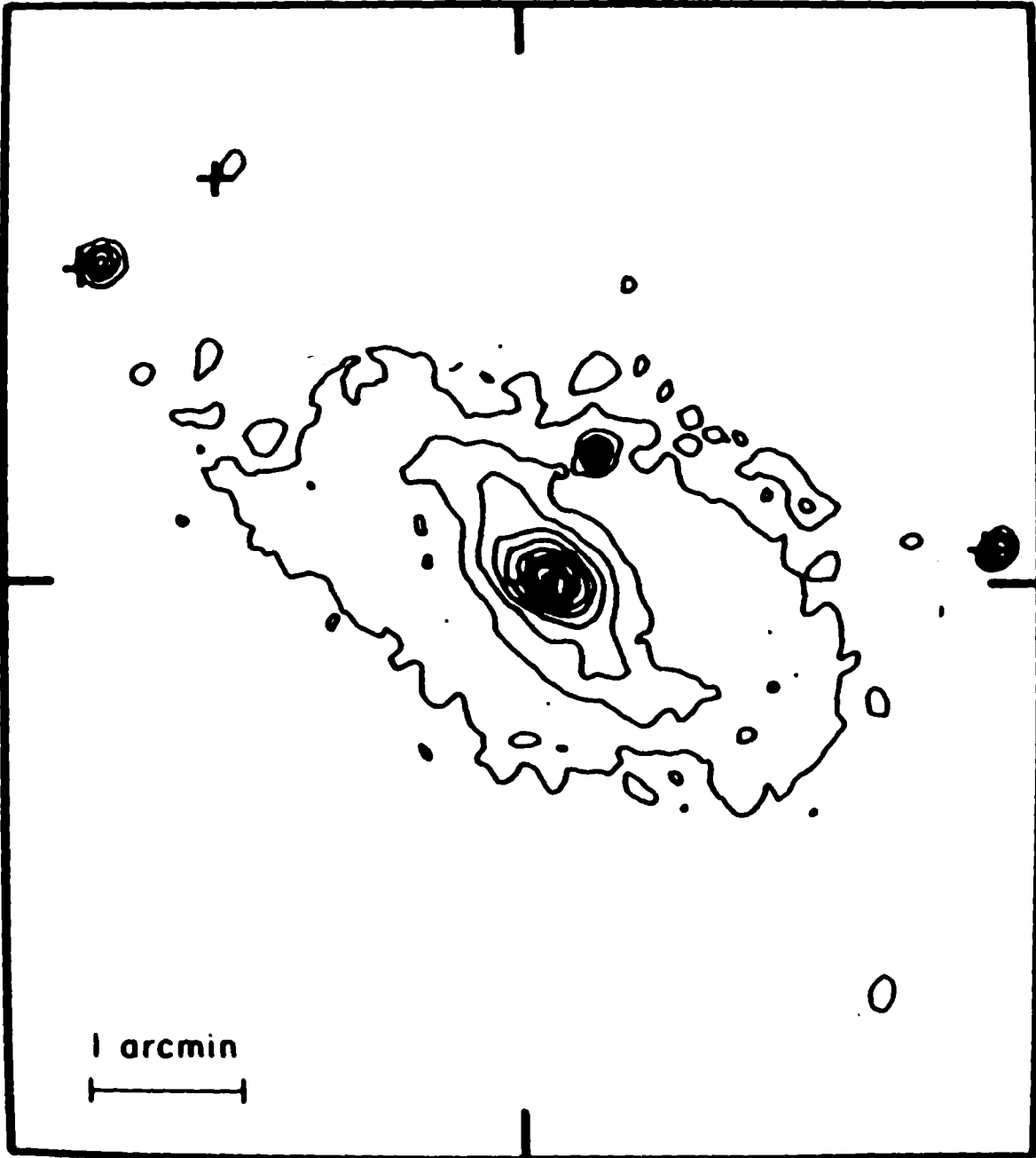


Figure 3

Figure 4

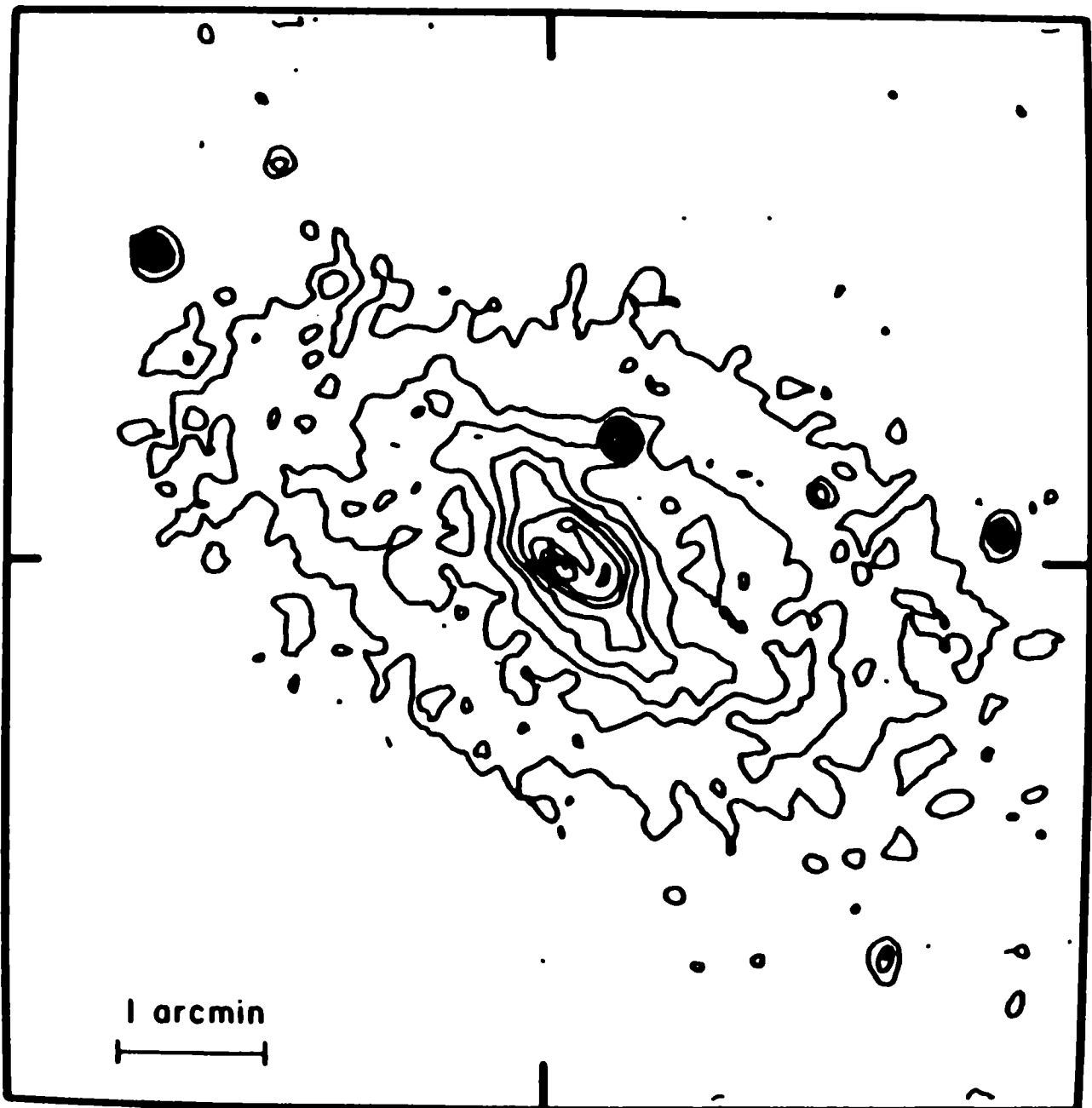


Figure 5

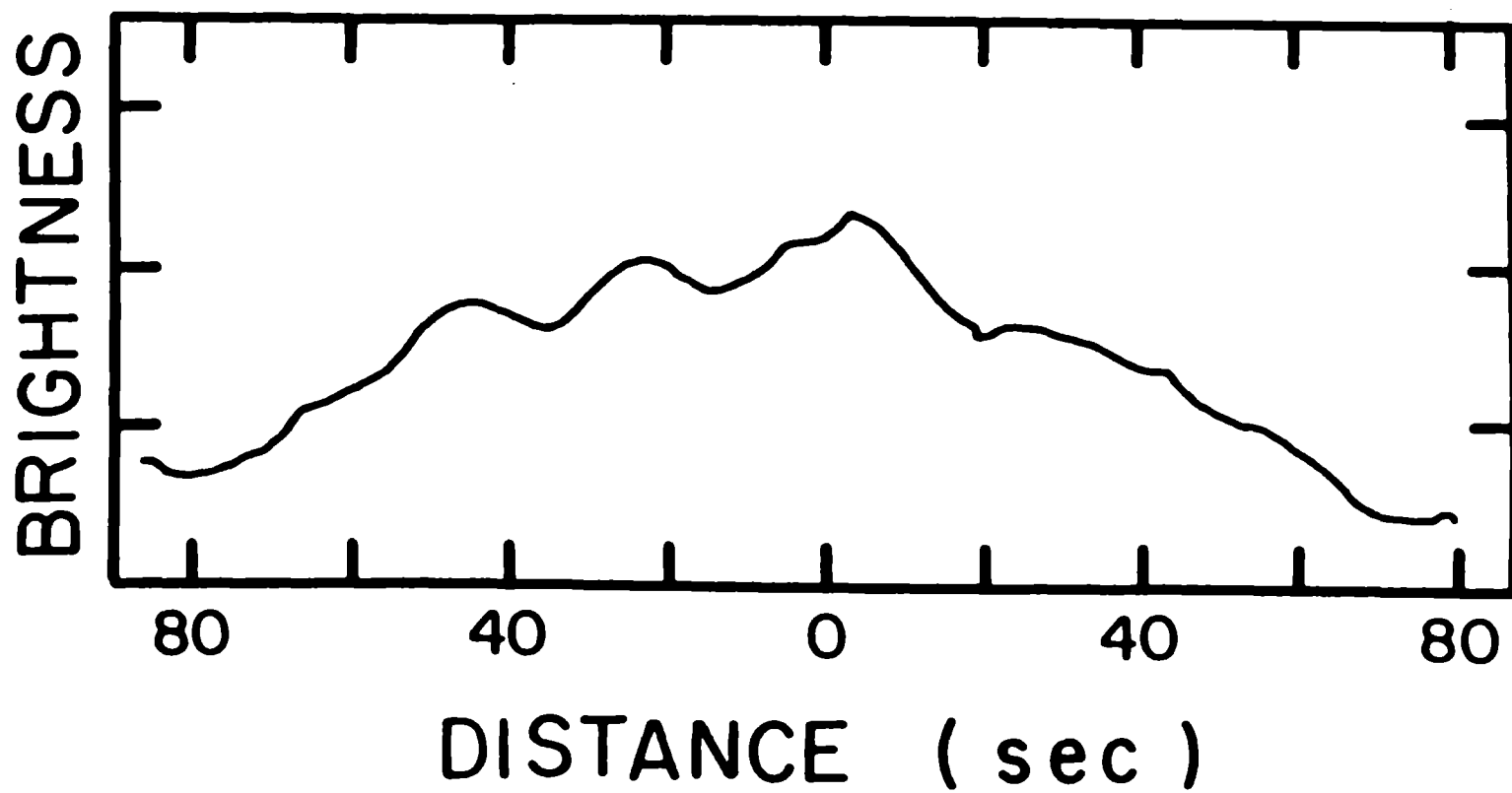
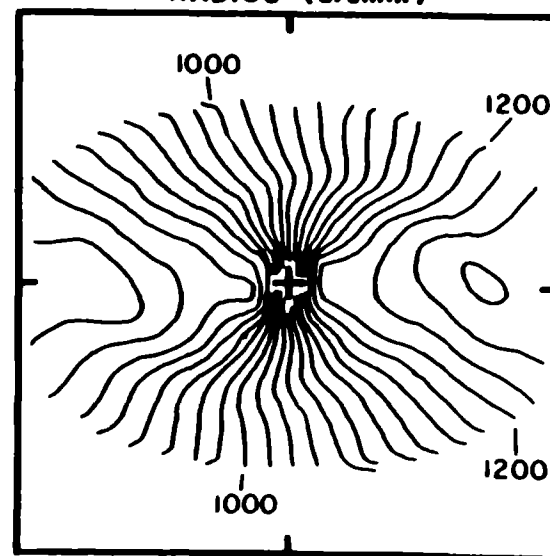
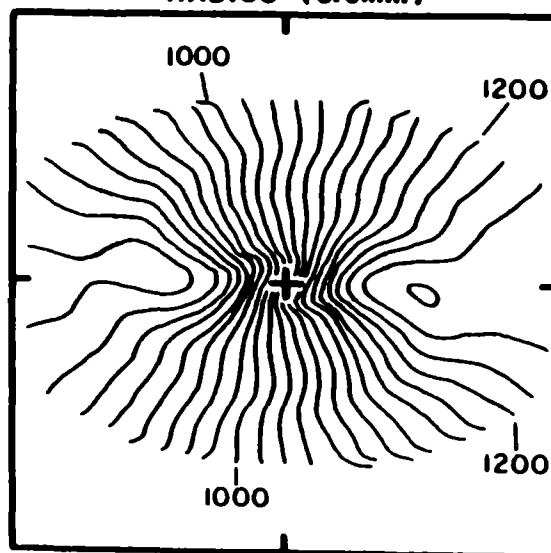
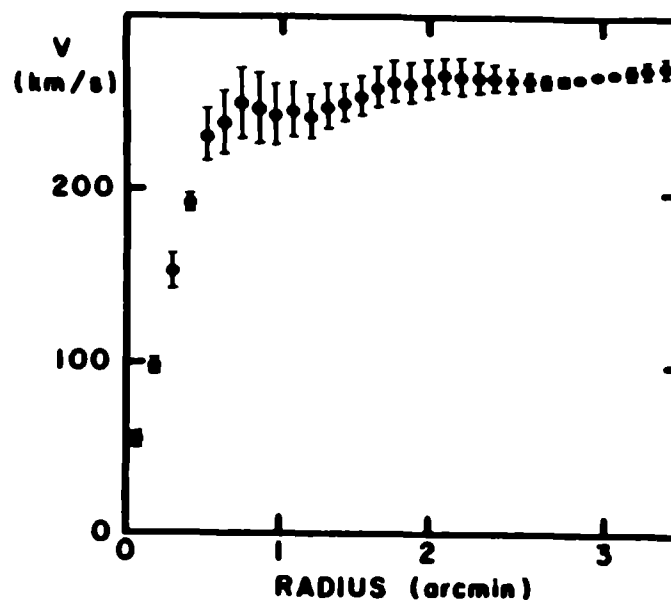
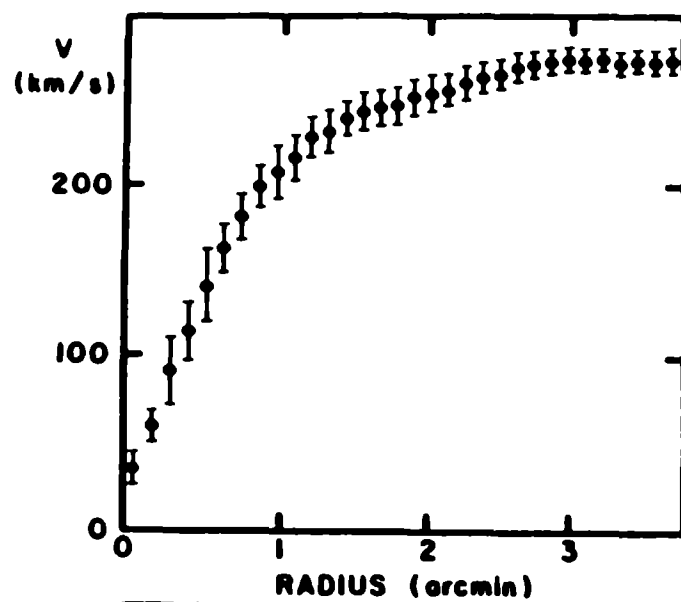


Figure 6



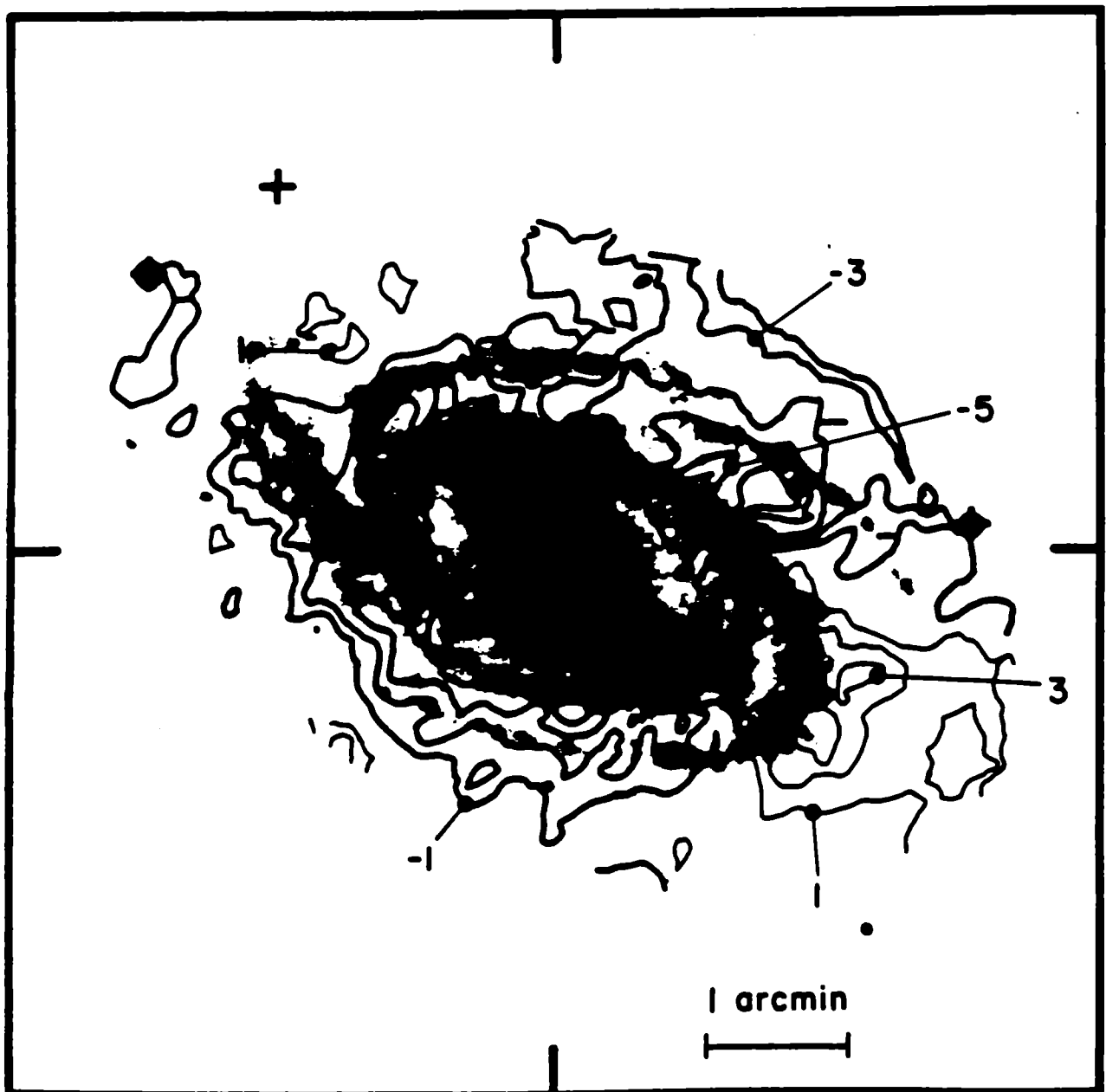
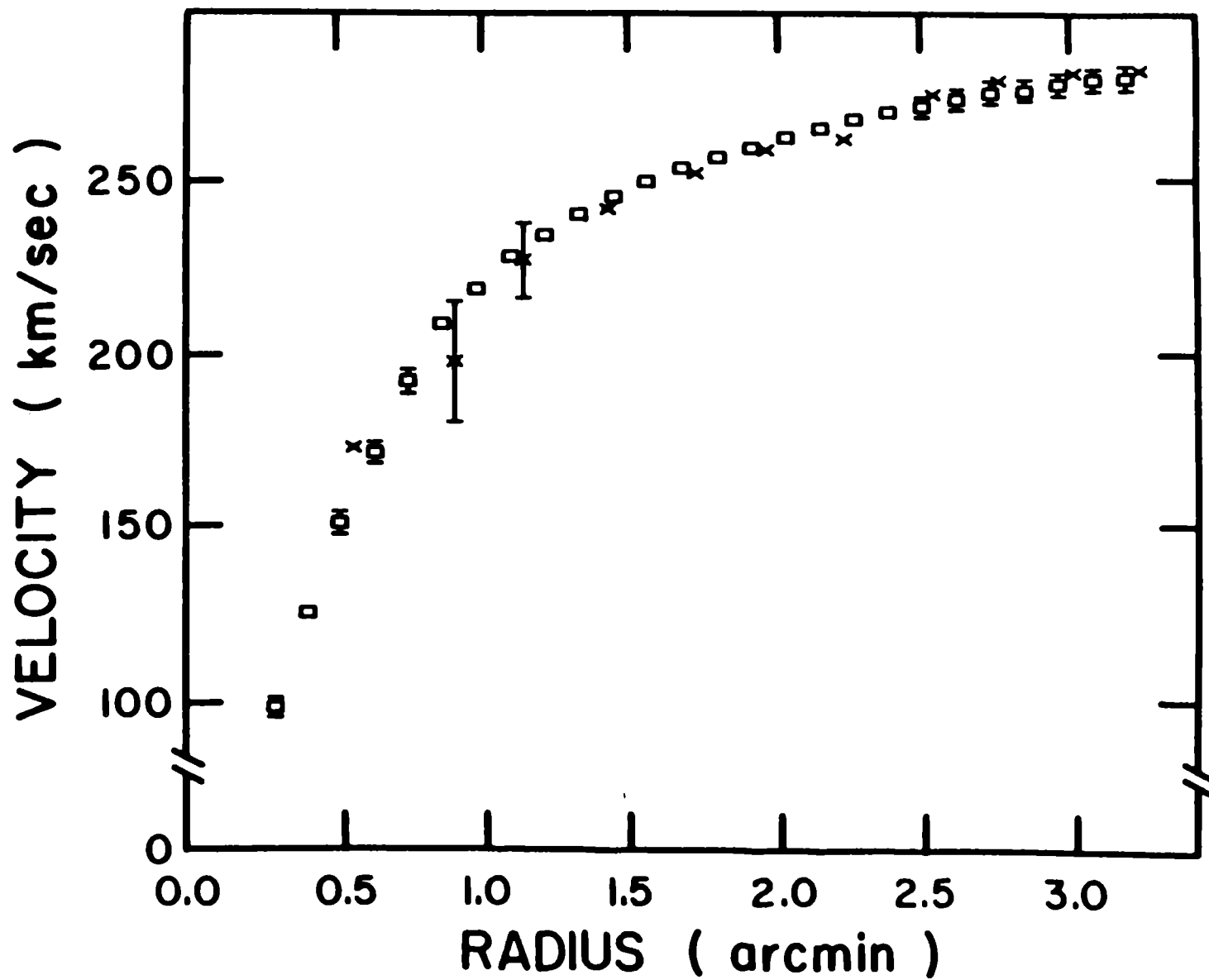


Figure 7

Figure 8



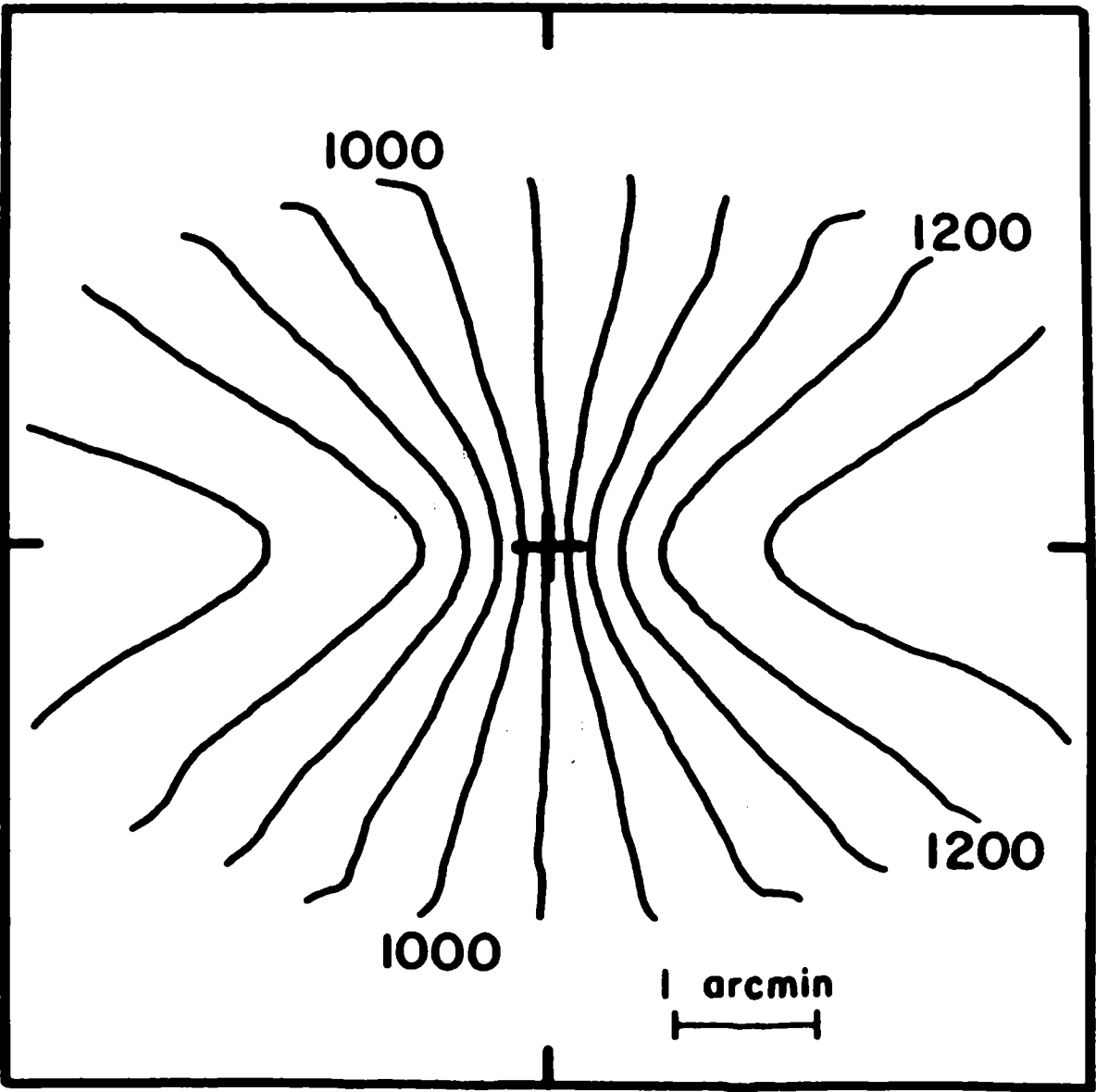


Figure 9

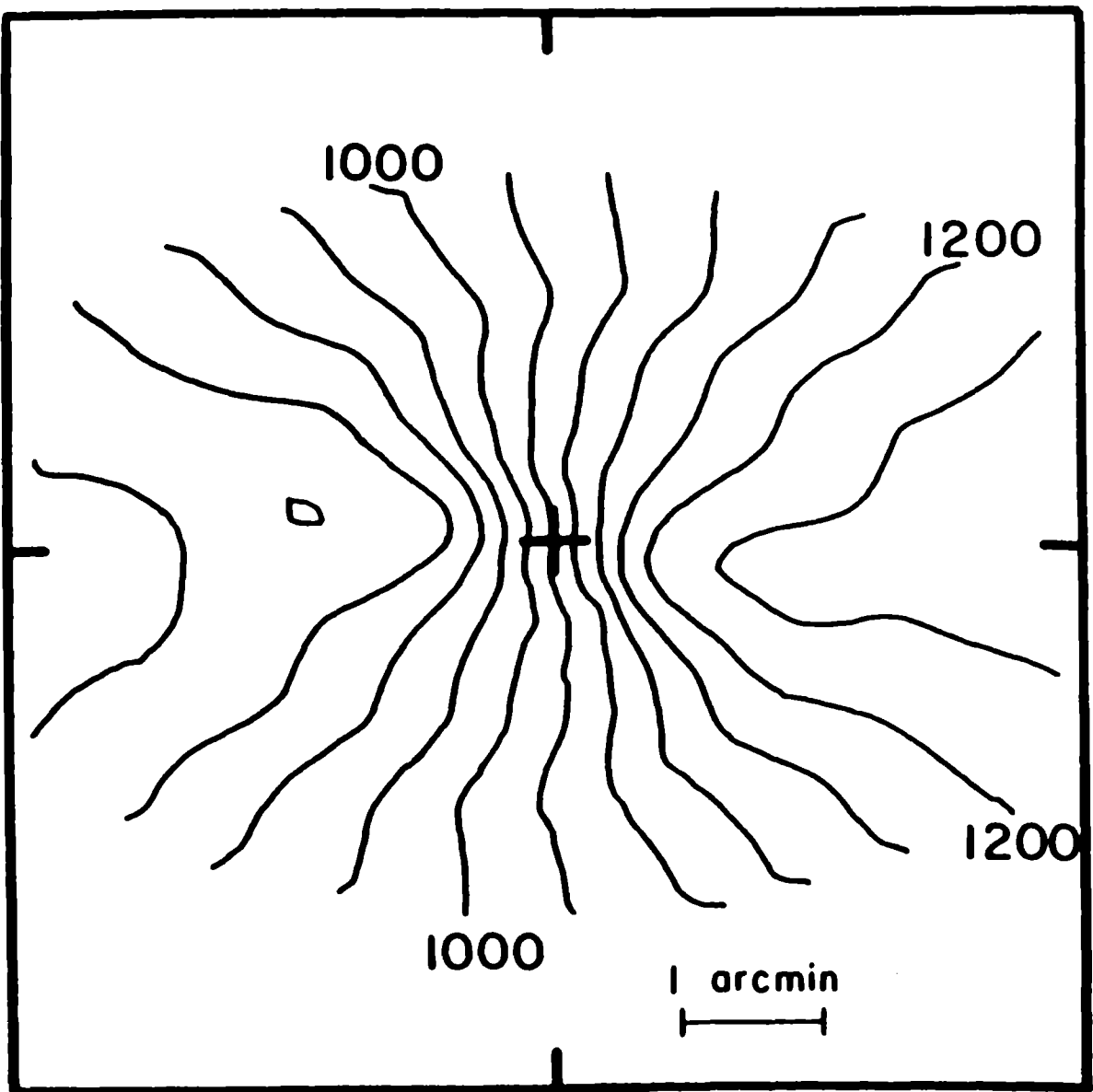
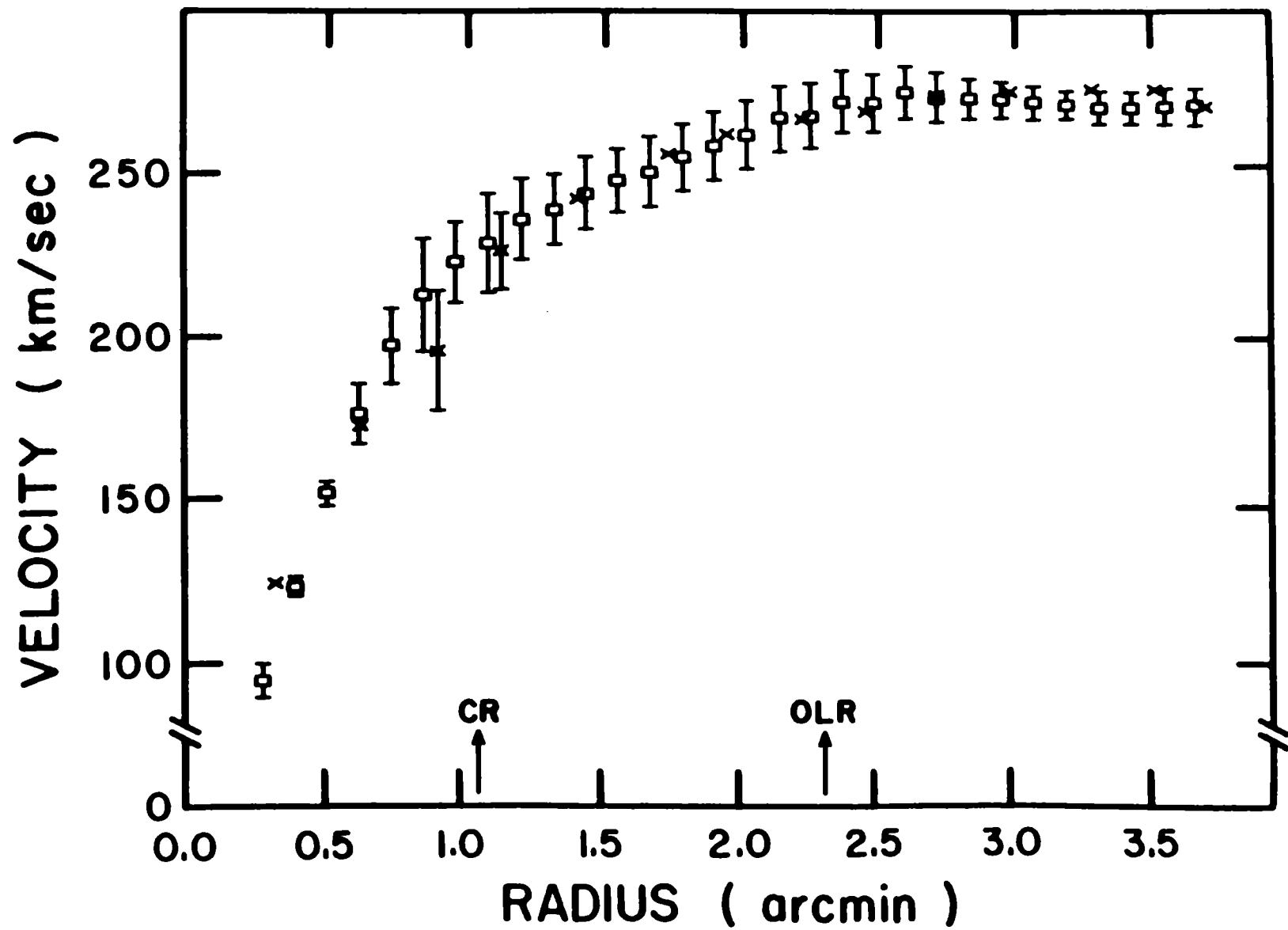


Figure 10

Figure 11



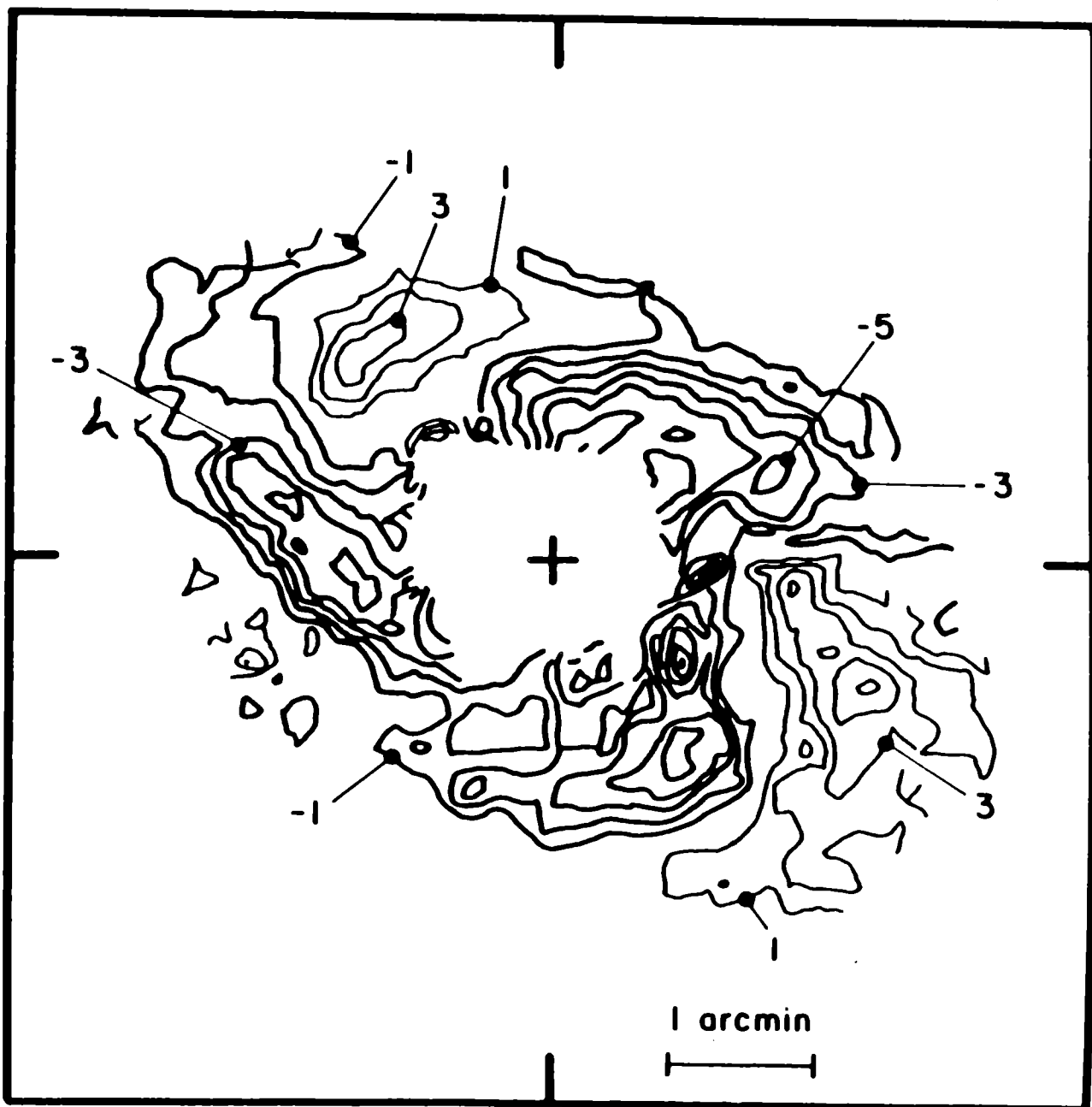


Figure 12

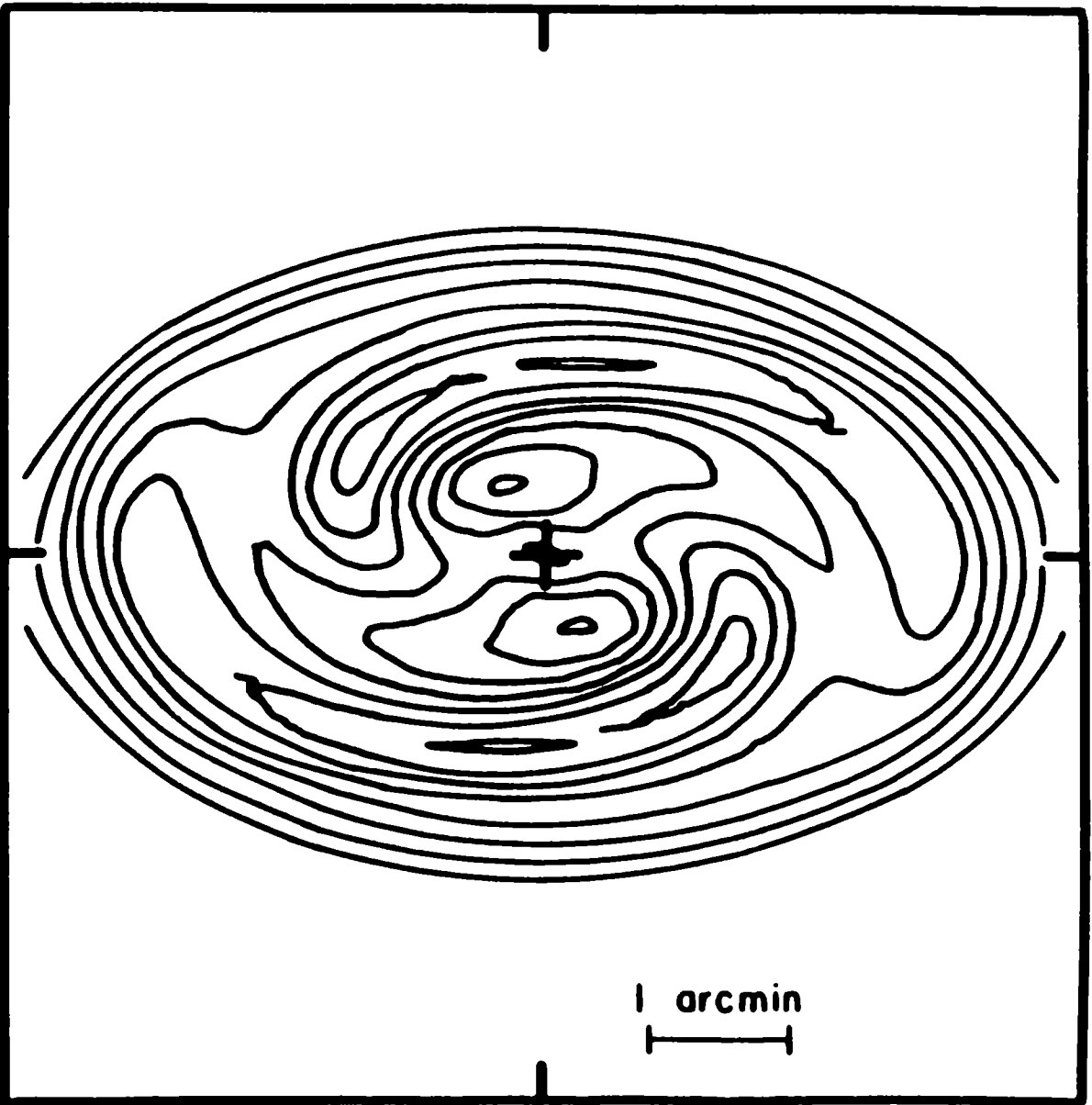
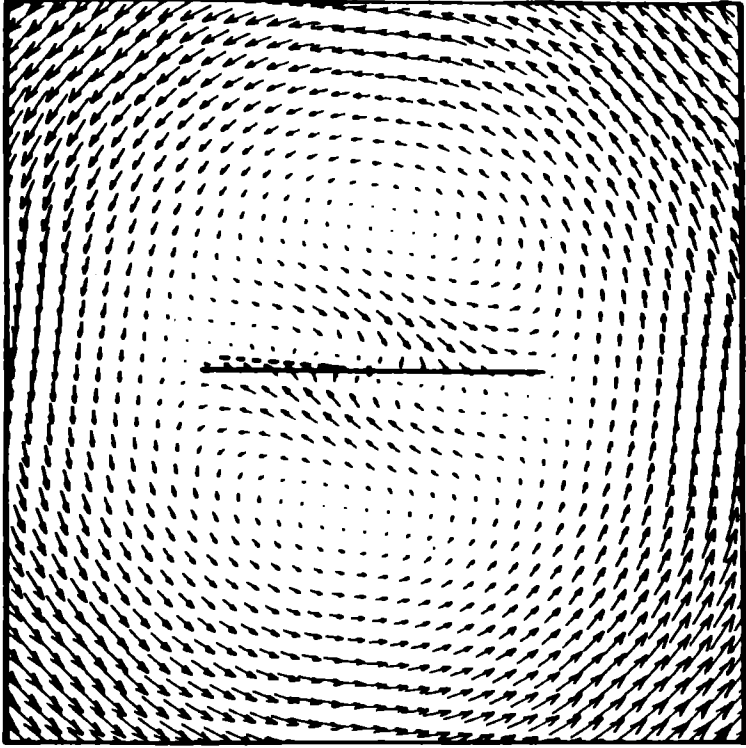


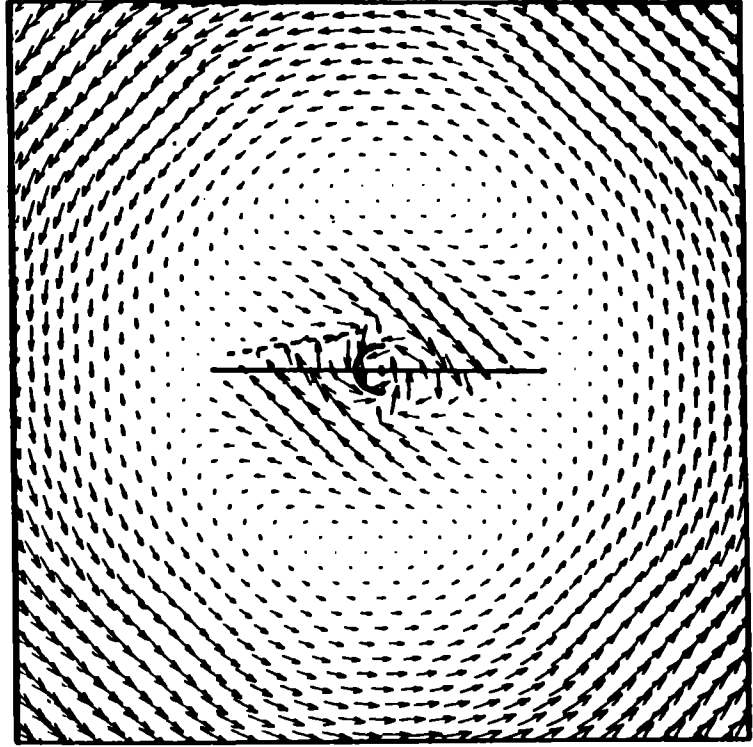
Figure 13



Figure 14



(a)



(b)

300 km/s

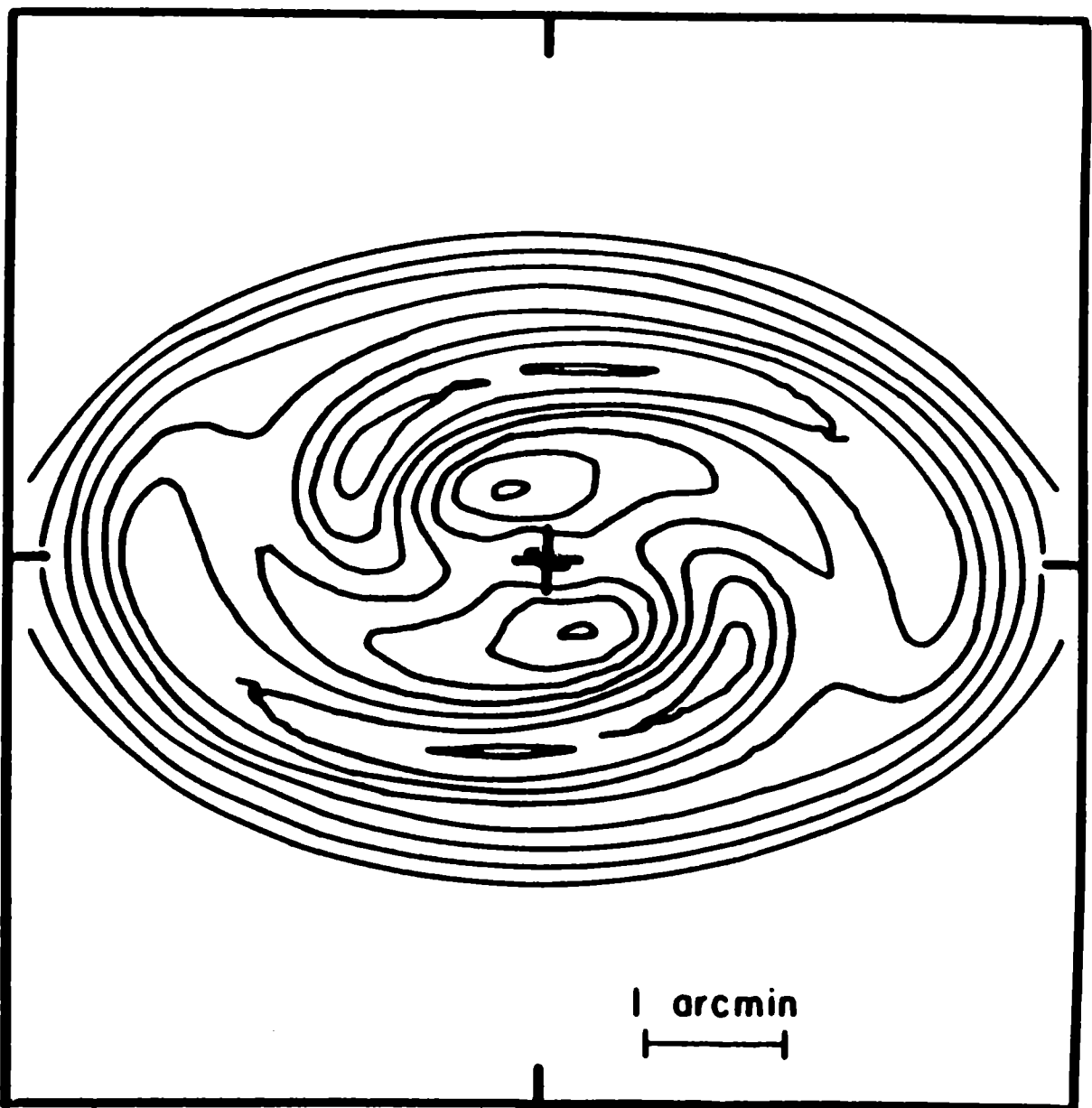


Figure 13

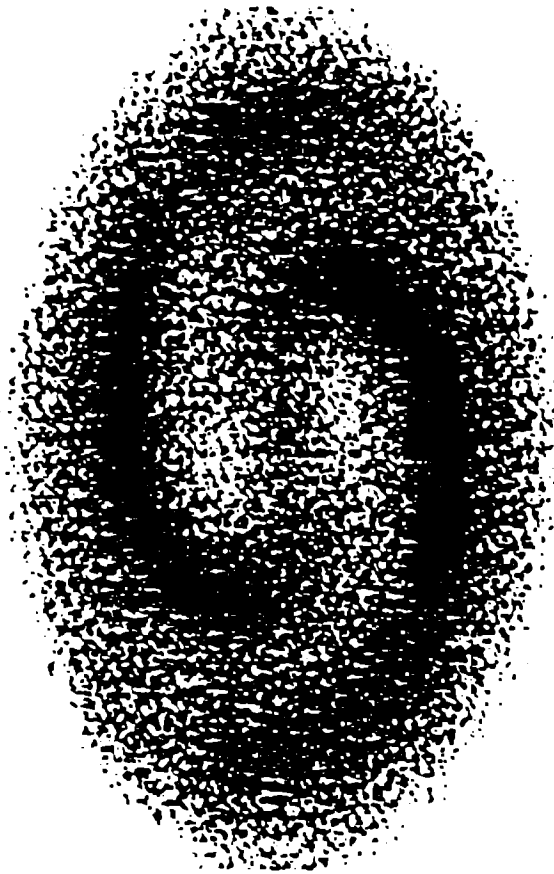
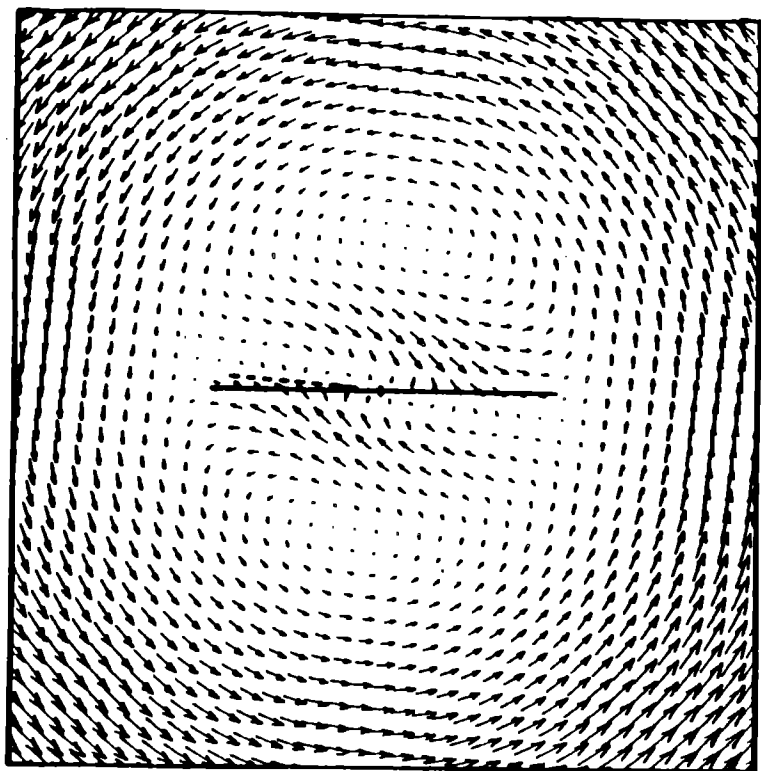
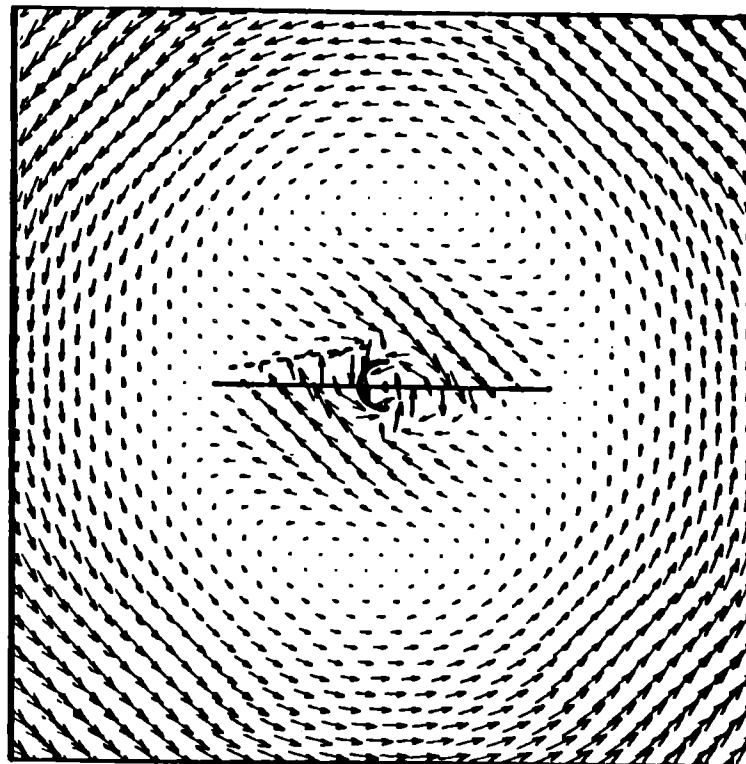


Figure 14



(a)



(b)

300 km/s